Master Thesis

Separating prompt and non-prompt dielectrons in pp collisions at $\sqrt{s}$ = 7 TeV with ALICE at the LHC

Sebastian Scheid

October 2016

Institut für Kernphysik
Goethe-Universität
Frankfurt am Main

Erstgutachter: Prof. Dr. Harald Appelshäuser
Zweitgutachter: Prof. Dr. Christoph Blume

DILEPTONEN ODER TOD

Abstract

The theory describing the interaction of colour-charged objects is called Quantum Chromodynamics (QCD). It predicts a state, for high temperatures and densities, in which the confinement is abrogated. This state is called a quark-gluon plasma (QGP). The observation of this state is not easily possible in nature, but can be achieved at large particle accelerators. Heavy nuclei can be collided in order to reach the required energy densities to form a QGP.

The most powerful accelerator built so far is the Large Hadron Collider (LHC) at the European Organization for Nuclear Research (CERN) in France and Switzerland. At the LHC, A Large Ion Collider Experiment (ALICE) is the dedicated experiment to observe and measure the properties of the QGP. The requirements for the experiment are a very good momentum and tracking resolution for up to 20000 particles flying through the detector and additionally achieving excellent particle identification possibilities. ALICE is well-suited to meet these demands.

A key observable to quantify bulk properties of the QGP is its temperature. Naively, this temperature can be accessed by measuring photons from the thermal radiation. The problem arises now in measuring these photons. A direct measurement has to deal with a huge background, limitations in the kinematic regime of the measurement, and a blueshift caused by the collective behaviour of the system. A remedy is to measure e^+e^- pairs originating from virtual photons from this radiation, which intrinsically overcome these shortcomings. The main background in this measurement stems from semi-leptonic decays of heavy-flavour hadrons. Luckily, the decay kinematics of these differ from the ones of the virtual photons which can be used to separate the contributions from each other.

In this thesis a method to distinguish e^+e^- pairs from heavy-flavour decays and virtual photons is developed and tested. Therefore we exploit secondary vertex information on the pair level in the analysis of pp data at $\sqrt{s} = 7$ TeV. Templates provided by Monte Carlo (MC) simulations are used to unfold the measured data and show the sensitivity of the method to separate prompt from delayed contributions. Finally, the consistency of the distributions from data with the hadronic cocktail is presented.

Contents

1. Introduction **1**

1.1. Standard Model of Particle Physics 1
1.2. QCD Matter 2
1.3. Quark-Gluon Plasma 4
1.4. Dielectrons as a Probe of the QGP 5
1.4.1. The Dielectron Continuum 5
1.4.1.1. Dalitz and Resonance Decays 7
1.4.1.2. Thermal Dielectrons 7
1.4.1.3. Correlated Pairs from Semi-Leptonic Heavy-Flavour Meson Decays 9
1.5. Pair Distance of Closest Approach 10

2. The LHC and ALICE **13**

2.1. Large Hadron Collider - LHC 13
2.2. A Large Ion Collider Experiment - ALICE 14
2.2.1. Inner Tracking System - ITS 14
2.2.2. Time Projection Chamber - TPC 15
2.2.3. Time Of Flight - TOF 18

3. Analysis **21**

3.1. Dataset and Monte Carlo 21
3.1.1. Dataset 21
3.1.2. Monte Carlo Production 21
3.1.3. Track Selection 22
3.2. Particle Identification 22
3.2.1. Electron Selection 23
3.2.1.1. ITS 23
3.2.1.2. TOF 23
3.2.1.3. TPC 23
3.3. Pairing of Electron Candidates 27
3.3.1. Pair Spectra 27
3.3.1.1. Prefilter track cuts 27
3.3.2. Signal Extraction 29

4. Template Distributions from Monte Carlo **32**

4.1. Template Construction 32
4.1.1. π^0-Mesons 32

4.1.2. J/ψ-Mesons . . . 33
4.1.3. D-Mesons . . . 35
4.1.4. B-Mesons . . . 36
4.2. Cocktail Comparison . . . 40
4.2.1. Pion Mass Region . . . 40
4.2.2. Resonance Mass Region . . . 40
4.2.3. Intermediate Mass Region . . . 41
4.2.4. J/ψ Mass Region . . . 42
4.3. Discussion . . . 44

5. Summary and Outlook **46**

A. Appendix **47**
A.1. Units . . . 47
A.2. Kinematics . . . 47
A.3. Coordinates in ALICE . . . 49
A.4. List of Runs . . . 49

Bibliography **52**

1. Introduction

1.1. Standard Model of Particle Physics

The four fundamental forces known until now are the strong, electromagnetic, weak force and gravity. The first three can by described by means of the standard model of particle physics. The fundamental particles included in the standard model are collected in fig. 1.1.

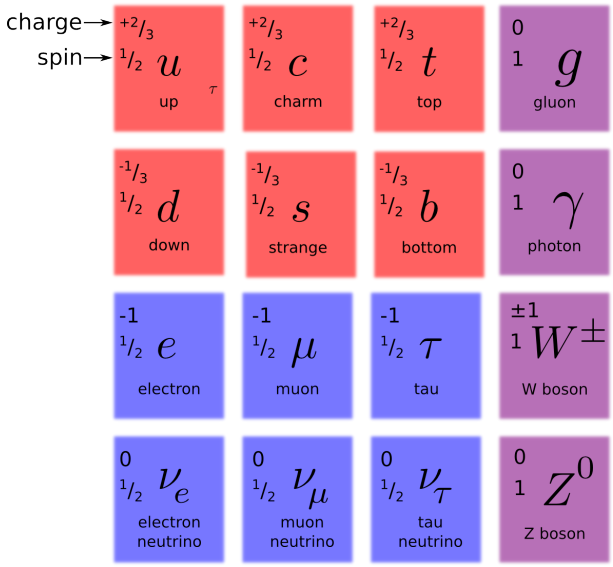

Figure 1.1.: Particles of the standard model. The gauge bosons are shown on the right, the quarks on the upper left and the leptons on the lower left.

The particles listed here can be divided into into fermions with spin $\frac{1}{2}$ and gauge bosons with spin 1. The gauge bosons are the particles mediating the interaction between the fermions of the standard model. The interactions in which each fermion takes part and by what boson it is mediated is summarized in tab. 1.1.
The fact that among the fermions only quarks interact strongly is due to the circumstance that only quarks and gluons carry colour charge. The dynamics of colour-charged - and thus strongly interacting - objects is described in the theory of Quantum Chromodynamics (QCD).

	Interaction (mediating boson)		
Fermion	strong (gluon)	electromagnetic (photon)	weak (W/Z)
Quarks	X	X	X
$e\ \mu\ \tau$		X	X
$\nu_e\ \nu_\mu\ \nu_\tau$			X

Table 1.1.: Interaction of elementary particles.

1.2. QCD Matter

Objects consisting of quarks and gluons are called hadrons. They all appear in a colour-neutral or white state. A colour-neutral state can be reached by either combining three quarks (a baryon) with the different colour red, blue and green or combining a quark and an anti-quark (a meson). The fact, that quarks only appear in bound states is called confinement. This can be explained by the potential $V(r)$ given by eq. 1.1

$$V(r) = \frac{-\alpha_s}{r} + k \cdot r \tag{1.1}$$

The potential consists of two terms. The first one is similar to the Coulomb potential. It dominates the potential at small distances r with the coupling constant of the strong interaction α_s. The second one is a linear term, that results from the fact that gluons carry colour charge and interact with each other. This leads to a different result in the propagation of the interaction than in the electromagnetic case. The force between two electric charges will get smaller for greater distances due to the $1/r$ potential. For strongly interacting matter this is not the case. The second term in the potential suggests that for a growing distance also the energy put into the system has to grow. At some point the energy will be enough to create a quark anti-quark pair and new colour-neutral objects are formed.

Another feature of QCD is the strong momentum transfer dependence of its coupling constant $\alpha_s(Q^2)$ which is given by eq. 1.2.

$$\alpha_s(Q^2) = \frac{12\pi}{(33 - n_f) \cdot \ln(Q^2/\Lambda^2)} \tag{1.2}$$

In this equation n_f reflects the number of quark flavours and Λ the scaling variable of QCD. As shown in fig. 1.2 α_s decreases with a rise in Q.

With Heisenberg's uncertainty principle one can relate the momentum transfer to the distance between two particles as $Q \sim 1/r$. This means that for either hard scattering processes or very small distances the coupling between the quarks and gluons gets weaker. This phenomenon is called asymptotic freedom. It was thought, that the weakening of the coupling would lead to a medium in which the quarks and glouns would not be bound into hadrons anymore and behave like a weakly interacting gas. It was however shown

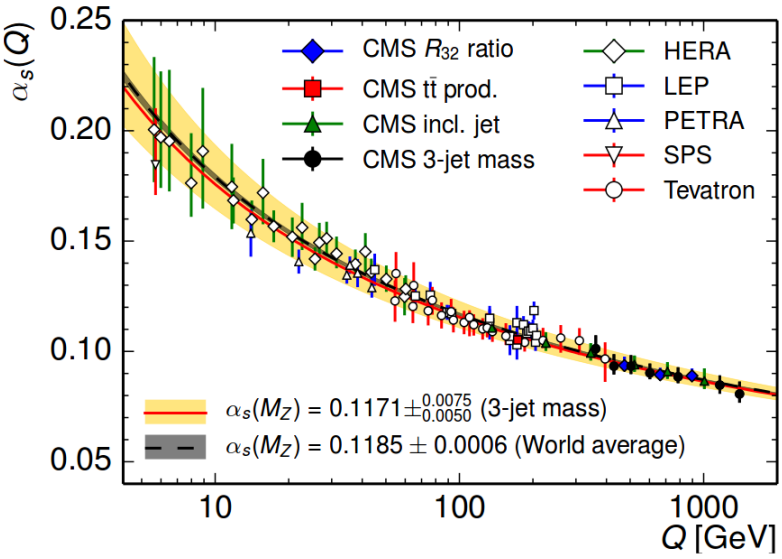

Figure 1.2.: Measurement of α_s by different experiments in different channels[CMS 15].

at RHIC that the observed matter is actually a strongly interacting quark-gluon plasma (sQGP)[NAG 07] and behaves like an almost perfect liquid [PHE 15]. This state of QCD matter where liberated quarks and gluons can be observed is believed to be reached for high temperatures and densities. The transition from hadronic matter, where the quarks and gluons are bound in hadrons, to partonic matter, is shown in 1.3.

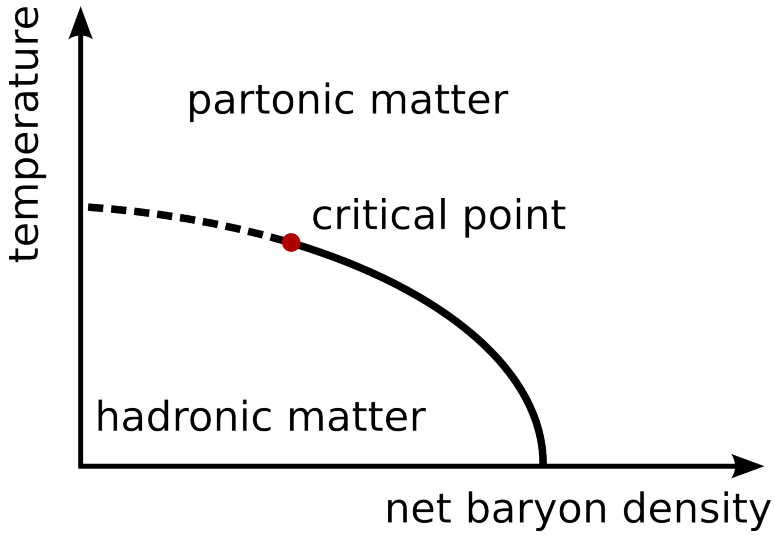

Figure 1.3.: Sketch of the phase diagram of strongly interacting matter. The solid line shows a first order phase transition from hadronic into partonic matter at large net baryon density. The phase transition changes from first order to a cross over with increasing temperature at a critical point [SRS 98].

In the phase diagram we see two different phase transitions. The first one at low temperature and high net baryon density is suggested to be a first order phase transition. At a temperature of about 170 MeV [1] and zero net baryon density, a cross over phase transition is expected [FK 04]. The two join at a critical point.

1.3. Quark-Gluon Plasma

As mentioned in the previous section the state of strongly interacting matter, where due to high temperatures or densities the hadronic structure is disolved and quarks and gluons are liberated, is called a quark-gluon plasma. If we want to study such a state, it has to be produced in the laboratory, since it is inaccessible in nature. This is done in ultrarelativistic heavy-ion collisions. A space-time representation of such a collision is shown in fig. 1.4.

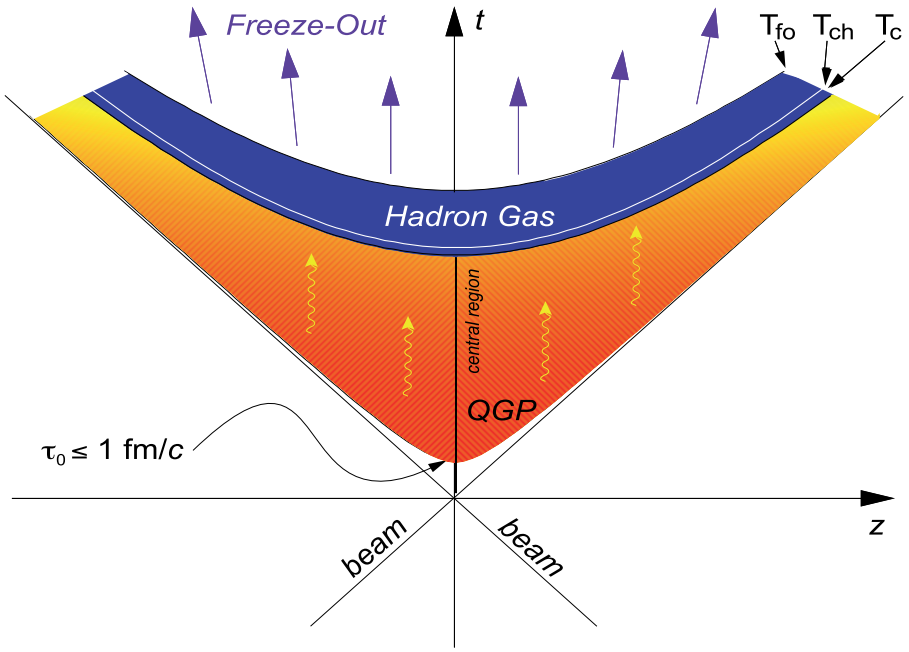

Figure 1.4.: Evolution of a heavy-ion collision in time and one spatial coordinate [KSSS 08].

In the sketch we can see that, after the nuclei collide, the medium needs a time τ_0 to form. After formation, the medium starts expanding and cooling down. If the critical temperature T_C is reached, the quarks and gluons start forming colour-neutral hadrons and a hot hadronic gas is generated. This gas also expands and cools further. At the point of chemical freezeout T_{ch} the particle composition of the hadron gas is fixed. The energy and momentum of the hadrons is not sufficient to collide inelastically any longer. Finally, at kinetic freezout, also the momentum spectra of the particles are fixed, no more

[1] A short introduction into units and kinematics used in this thesis is given in A.1 and A.2

interaction is happening and the particles stream freely into the detectors where they are measured. We can see here that the final-state hadrons interact strongly with each other until the very late stage of the collision. This leads to a loss of information about the early stages of the collision and complicates the study of the properties of the deconfined medium. One way to overcome this problem is to look into probes that do not interact strongly.

1.4. Dielectrons as a Probe of the QGP

Probes that do not strongly interact with the medium are electromagnetic probes, these being photons and leptons.
Real photons are emitted by a hot and expanding medium and the expansion of the source of the photons leads to a blue shift. This blue shift modifies the energy spectrum of the photons and therefore inhibits, e.g., the unambiguous extraction of the temperature of the source. Another way of measuring the QGP-induced electromagnetic radiation is via the dielectron channel. This has some major advantages. For one, the dielectron channel gives access to the virtual photon production via the measurement of the pair's invariant mass, which is defined as

$$m_{inv}^2 = (P_1 + P_2)^2 = (E_1 + E_2)^2 - (\mathbf{p}_1 + \mathbf{p}_2)^2 \tag{1.3}$$

where P_i are the 4-momentum vectors of the particles, E_i their energy and $\mathbf{p}_i$ their 3-momentum. This observable is Lorentz-invariant and is not affected by the medium's expansion. A second reason would be that the momentum of a pair is reconstructed from the decay products what makes it possible to measure down to the lowest momentum. As will be shown, the possibility of looking into the spectrum in different invariant mass ranges gives the possibility to probe different collision stages.

1.4.1. The Dielectron Continuum

If we want to measure virtual photons in the dielectron channel we have to develop a very good understanding of all the sources that lead to a dielectron pair which we will measure in the detector. The different sources we expect are shown as a sketch in fig. 1.5.
The light-flavour regime is dominated by the vector resonances ρ, ω, and ϕ and the pseudoscalar π^0, η, and η'.
Their lifetimes range from few tens of yoctoseconds of the strongly decaying ρ to a tenth of a femtosecond of the electromagnetically decaying π^0, which yields decay lengths on the sub-micrometer scale, see tab. 1.2. Similarily, it follows from the uncertainty principle that a virtual photon with a mass of 1 GeV/c^2, typical for this analysis, has to decay within a tenth of a fermi. All of these processes fall beyond state-of-the-art resolution

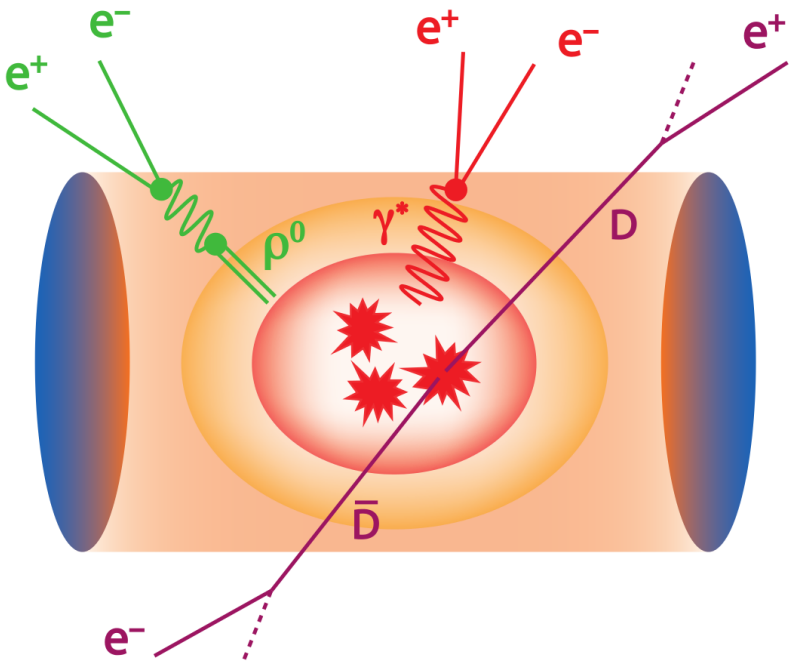

Figure 1.5.: Sketch of different sources of dielectrons [REI 16]

	lifetime	$c\tau$
light flavour		
ρ	$4.41 \cdot 10^{-}23$ s	13 fm
ω	$7.75 \cdot 10^{-}23$ s	23 fm
ϕ	$1.54 \cdot 10^{-}22$ s	46 fm
η'	$3.32 \cdot 10^{-}20$ s	10 pm
η	$5.02 \cdot 10^{-}19$ s	150 pm
π^0	$8.52 \cdot 10^{-}17$ s	26 nm
heavy flavour		
J/ψ	$7.09 \cdot 10^{-}21$ s	769 fm
$D^{\pm}$	$1.04 \cdot 10^{-}12$ s	312 μm
$B^{\pm}$	$1.64 \cdot 10^{-}12$ s	491 μm

Table 1.2.: Lifetime and decay length of main dielectron sources [CPC 14]

capabilities and as such are experimentally indistinguishable.

The heavier masses of the continuum are populated by the heavy-flavour part of the spectrum. On the one hand there is the J/ψ which also decays electromagnetically and very fast. On the other hand there are so-called open heavy-flavour mesons, the D- and B-mesons. They consist of one charm or beauty and one light-flavour quark. These can only decay in channels of the weak interaction since the strong and electromagnetic force have to conserve the quark flavours. In contrast to strong and electromagnetic decays, lifetimes of weakly decaying particles are long. This leads to a macroscopic decay length,

see also tab. 1.2, and a decay point that can be separated from the primary event vertex for the open heavy-flavour mesons.

1.4.1.1. Dalitz and Resonance Decays

The largest contribution to the di-electron spectrum at low masses stems from Dalitz decays of the π^0 and η-meson. The main decay channel for π^0 is the decay into two photons with a branching ratio of 98.8% [CPC 14]. These are not measured in the di-electron spectrum except for conversions of these photons in the detector material as contamination. The 1.2% remaining π^0 decay almost exclusively via one real and one virtual photon where the virtual photon disintegrates into an e^+e^- pair. This decay is called a Dalitz decay and its underlying process is called internal conversion. Its probability and the shape of the mass spectrum were calculated and parametrized by N. M. Kroll and W. Wada [KW 55]. The mass distribution is given by 1.4 [SSS 10].

$$\frac{\mathrm{d}^2 n_{\mathrm{ee}}}{\mathrm{d}^2 m_{\mathrm{ee}}} = \frac{2\alpha}{3\pi}\frac{1}{m_{\mathrm{ee}}}\sqrt{1-\frac{4m_{\mathrm{e}}^2}{m_{\mathrm{ee}}^2}}\left(1+\frac{2m_{\mathrm{e}}^2}{m_{\mathrm{ee}}^2}\right) S\mathrm{d}n_\gamma. \tag{1.4}$$

Here $m_{\mathrm{ee}}$is the invariant mass of the e^+e^- pair, m_{e} the electron mass, α the electromagnetic coupling constant and S a process-dependent variable. For virtual photons the approximation $S \approx 1$ is made. This simplification, which corresponds to a point-like process, holds for $m_{\mathrm{ee}} \ll p_{\mathrm{T,ee}}$, where $p_{\mathrm{T,ee}}$ is the length of the vectorial sum of the single electron transverse momenta. For the decay of a hadron with mass M_h, S can be calculated as $S = |F(m_{\mathrm{ee}}^2)|^2(1 - m_{\mathrm{ee}}^2/M_h^2)$, where F is the relevant form factor and $(1 - m_{\mathrm{ee}}^2/M_h^2)$ describes the phase-space dependence.
We can already see that the Dalitz pair will not carry the whole invariant mass of the π^0 or η since only the momentum of both the electrons is taken into account, but the photon momentum is not. This will result in a continuous shape for the spectrum. The resonances, on the other hand, can decay directly into an e^+e^- pair. When calculating the invariant mass we will then always get a peak in the invariant mass spectrum.

1.4.1.2. Thermal Dielectrons

As we expect the creation of a very hot and dense medium also thermal radiation of this medium is predicted. Similar to electrons from Dalitz decays, there is a chance that the thermal photon is a virtual photon and can be measured in the dielectron channel. The medium will cool down over time which implies a change in the photon spectrum. In fig. 1.6 the yield for different energies of two collision systems is shown [EHB 16]. These are divided in an inclusive photon yield and a yield for the hot part of the emitting source. One can easily deduce, that the early stage of the medium evolution is dominated by high temperatures. This is also the part, where a QGP is expected. With this in mind we can

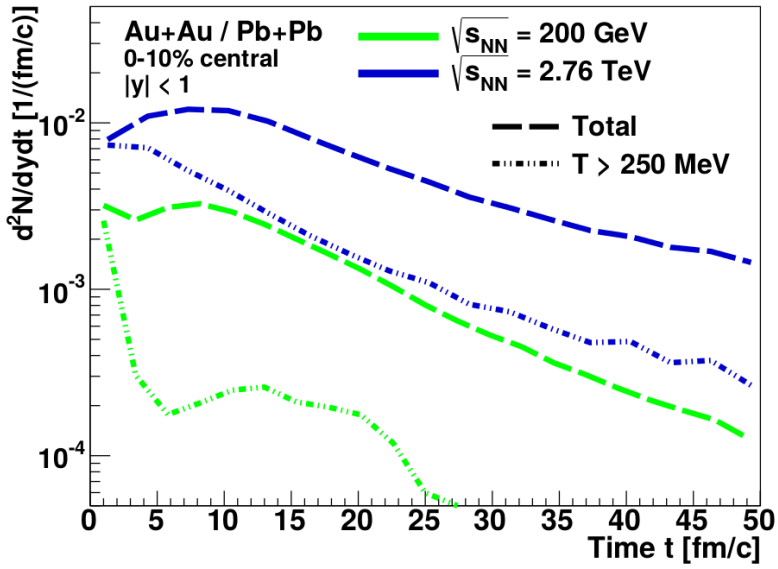

Figure 1.6.: Dielectron yield from virtual thermal photons as a function if the systems lifetime. The contribution from the hot parts of the system dominate the early phase of the collision [EHB 16].

see from fig. 1.7 that the hotter the medium is, the more mass the virtual photon will have [RAP 11].

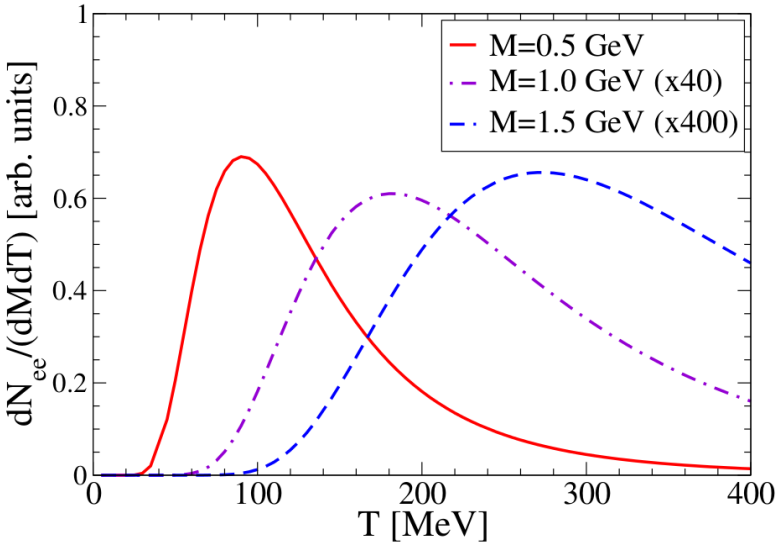

Figure 1.7.: Temperature profile for dielectrons from different virtual photon masses. Higher temperatures lead to larger virtual photon masses [RAP 11].

This is a unique opportunity the measurement in the dielectron channel gives us. If one would do this measurement for real photons one could only look into a blueshifted averaged

temperature of the different collision phases. The correlation of pair mass and temperature gives the possibility to directly look into the early phase of the collision.

1.4.1.3. Correlated Pairs from Semi-Leptonic Heavy-Flavour Meson Decays

In the same mass region where the thermal dielectrons from the early collision stages are expected there is also a very large contribution from the semi-leptonic decays of open heavy-flavour mesons. Semi-leptonic means that these mesons decay with leptons and hadrons in the final state. For D-mesons it is most likely that associated with the charged lepton a kaon as well as a neutrino to conserve the lepton number will be produced. B-mesons will most probably decay into a D-meson, a charged lepton and a neutrino. Examples for semi-leptonic decays are given in eq. 1.5, 1.6 and 1.7.

$$D^0 \rightarrow K^- e^+ \nu_\mathrm{e} \tag{1.5}$$

$$\bar{D^0} \rightarrow K^+ e^- \bar{\nu_\mathrm{e}} \tag{1.6}$$

$$B^0 \rightarrow D^- e^+ \nu_\mathrm{e} \tag{1.7}$$

These are 3-body decays with the decay hadron being orders of magnitude heavier than the other products. Therefore, the momentum destination of the electron is expected to be almost isotropic. Nevertheless, the quark-antiquark pair is produced together and when the quarks form hadrons they keep a correlation which finally is transferred to the $\mathrm{e^+e^-}$pair. The pairs reconstructed from these heavy-flavour electrons and positrons will predominantly populate the dielectron mass spectrum between the ϕ and the J/ψ mass peak. In this region a measurement of thermal dielectrons would be severely obstructed by the heavy-flavour contribution. Thus, it is necessary to establish a method to separate the heavy-flavour part from the thermal dielectrons. One would be an exact measurement of the production cross section and then simply subtract the expected contribution from charm. In fig. 1.8 charm cross section measurements for various energies are shown. For the subtraction approach an exact measurement would be needed. As indicated by the uncertainties in fig. 1.8 this is a challenging measurement. Therefore, we follow a different approach and accomplish the separation of the charm contribution and the signal from virtual photons by using the pair distance of closest approach DCA_ee which will be explained in detail in the next section.

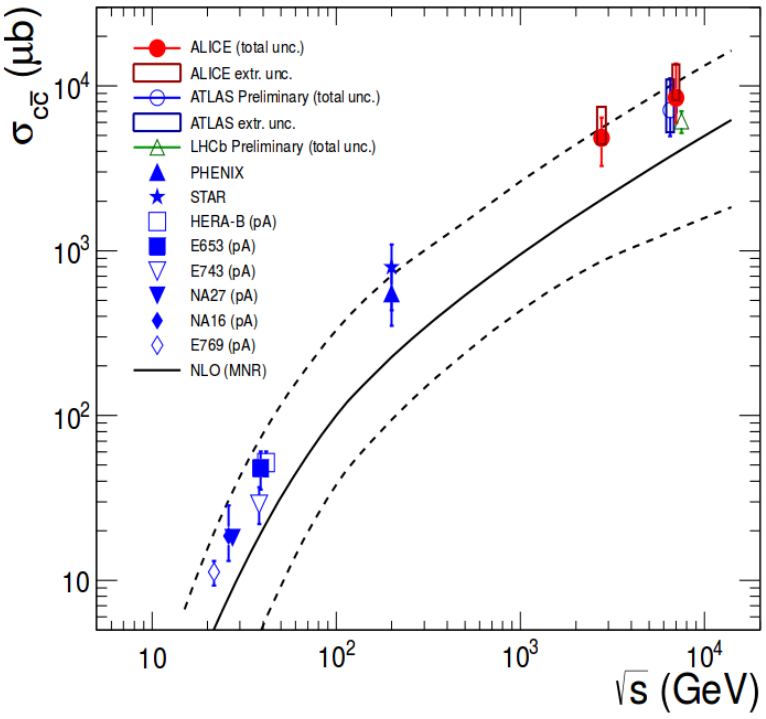

Figure 1.8.: Measurements of the $c\bar{c}$ cross section as a function of $\sqrt{s}$ [ALIb 12].

1.5. Pair Distance of Closest Approach

The distance-of-closest-approach (DCA) should be sensitive to the finite decay length of the heavy-flavour mesons. The construction of this variable is quite simple and a sketch is shown in fig. 1.9. We take the smallest distance of the extrapolation of a measured track to the reconstructed collision point.

The resolution of these tracks depends on their transverse momentum. Therefore we normalize each single-track DCA to its momentum-dependent resolution. This procedure guarantees independency from resolution effects. The pair variable DCA_{ee}we then calculate following the prescription given by the NA60 collaboration [NA60 08]:

$$DCA_{ee} = \sqrt{\frac{DCA_1^2 + DCA_2^2}{2}}. \tag{1.8}$$

As mentioned before the D- and B-mesons have a larger lifetime than the other sources contributing to the dielectron spectrum. This leads to the fact that the heavy mesons will move away from the initial collision before they decay. This is illustrated in fig. 1.5 where also the resonances and the virtual photons are indicated as decaying directly. Following these considerations, the open heavy-flavour should produce larger DCA_{ee}values than the light-flavour sources or the virtual photons. This can easily be understood by looking

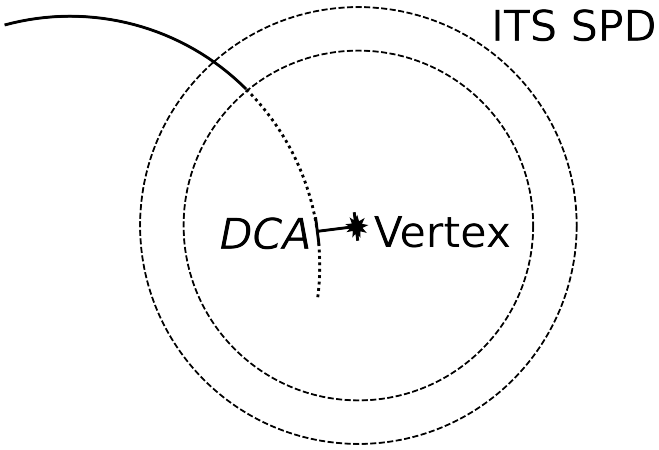

Figure 1.9.: Schematic drawing of a track measured in the detector. The actual measured space points begin in the first detector layer (dashed circles).The track then is reconstructed using the measured points (solid line) and extrapolated (dashed line) to estimate the DCA.

into fig. 1.10. On the left we see a sketch of a prompt decay with both legs originating

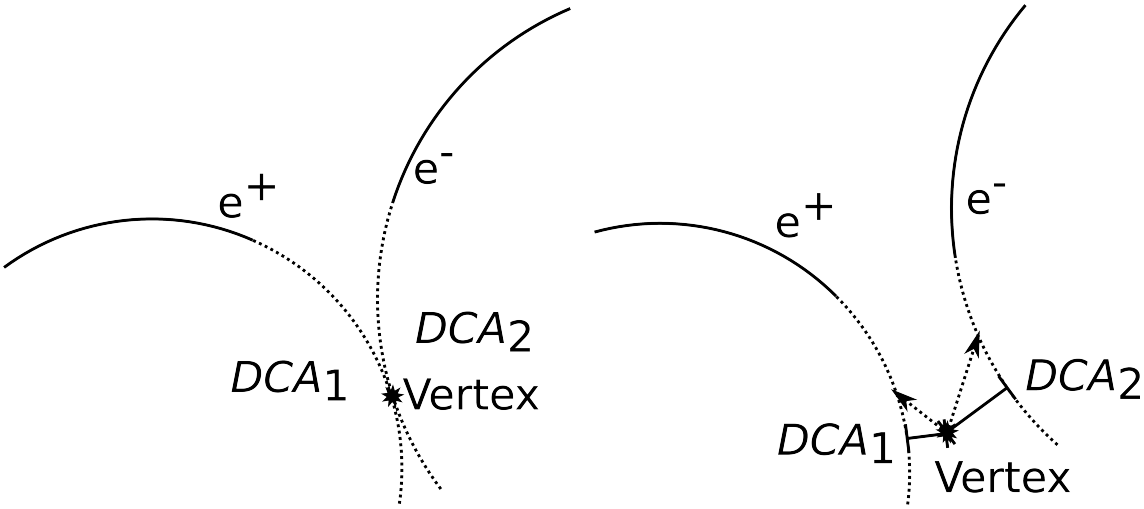

Figure 1.10.: Schematic of electrons and positrons from decays and their DCA. On the left for a prompt decay, on the right from two non-prompt decays of particles indicated by dashed arrows.

directly from the vertex. The reconstructed tracks will then also point to the vertex and in most cases a small DCA_{ee}will be calculated. On the right we see a scheme of two open heavy-flavour mesons decaying away from the primary vertex. The delayed decay in combination with the decay kinematics make it likely that the heavy-flavour decay electrons do not point to the primary vertex. This will lead to a larger DCA_{ee}value and in the end to a harder DCA_{ee} spectrum, as it was shown by the NA60 collaboration in fig.

1.11. Due to excellent vertex tracking capabilities it was possible to successfully separate the heavy flavour from the prompt part of the spectrum.

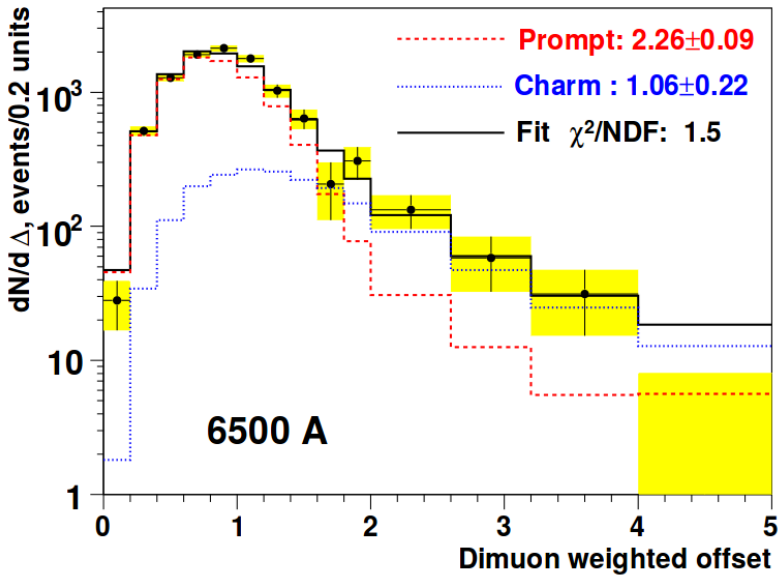

Figure 1.11.: Measurement of 158 AGeV In-In collisions in the 1.16-2.56 GeV/c^2 mass range by the NA60 collaboration. Templates extracted for a prompt and a charm part describe the measured spectra within uncertainties in terms of the dimuon weighted offset which is similar to DCA_{ee}[NA60 08].

Here we can see, that the measured spectrum can be described by two different contributions. This did show that a measured excess, that was also seen in other experiments, was indeed a prompt source and not as speculated an enhancement of D-meson production [LMW 95] going from nucleon-nucleus (p-A) to nucleus-nucleus (A-A) collisions.
After an introduction into the theory, explaining the effects exploited in this analysis and motivating the main observable DCA_{ee}, we now will continue with a description of the ALICE apparatus and more details on the main detectors used in this analysis. The third and fourth chapter contain the main analysis steps and a comparison of the obtained data to model calculations with a discussion of the results. In the last chapter a short summary and perspectives on future measurements are given.

2. The LHC and ALICE

In this chapter I will briefly introduce the more technical parts that lead to this analysis. It will mention the possibilities the accelerator provides and also introduce the capabilities of the detector.

2.1. Large Hadron Collider - LHC

The Large Hadron Collider (LHC) is the worlds largest collider. It was built in the old Large Electron Positron (LEP) collider tunnel at the European Center for Nuclear Research (CERN) in Switzerland and France. It consists of two separate beamlines fit together into an arrangement of superconducting magnets with their cooling system and other support structures. The accelerator can provide several collision systems at various energies. They are summarized in tab. 2.1. There are four experiments located at different

	Collision System	Center of Mass Energy
RUN1	pp	900 GeV, 2.36 TeV, 2.76 TeV, 5.02 TeV, 7 TeV, 8 TeV
2009-2013	pPb	5.02 TeV
	Pb–Pb	2.76 TeV
RUN2	pp	5.02 TeV, 13 TeV *
2015-2018	pPb	*
	Pb–Pb	5.02 TeV *
RUN3	pp	*
2021-2023	pPb	*
	Pb–Pb	*

Table 2.1.: Summery of the various collisions systems and center of mass energies at the CERN LHC. Marked with an asterisk (*) are entries where more measurements are expected in the future and the center of mass energy is not yet final.

interaction points (IP) at the LHC. These are the points where the beams are intersected with each other and thus brought to collision. ATLAS and CMS are specialized in the detection of new particles like the Higgs boson, which they found in 2012 [ATL 12][CMS 12], or supersymmetric particles. LHCb is mainly interested in the physics of heavy quarks and precisely measuring CP violation. The fourth experiment is ALICE.

2.2. A Large Ion Collider Experiment - ALICE

ALICE is the acronym for **A** **L**arge **I**on **C**ollider **E**xperiment. It is the only dedicated heavy-ion experiment at the CERN LHC. It provides excellent tracking and particle identification possibilities. A sketch with all detector systems is shown in fig. 2.1. The

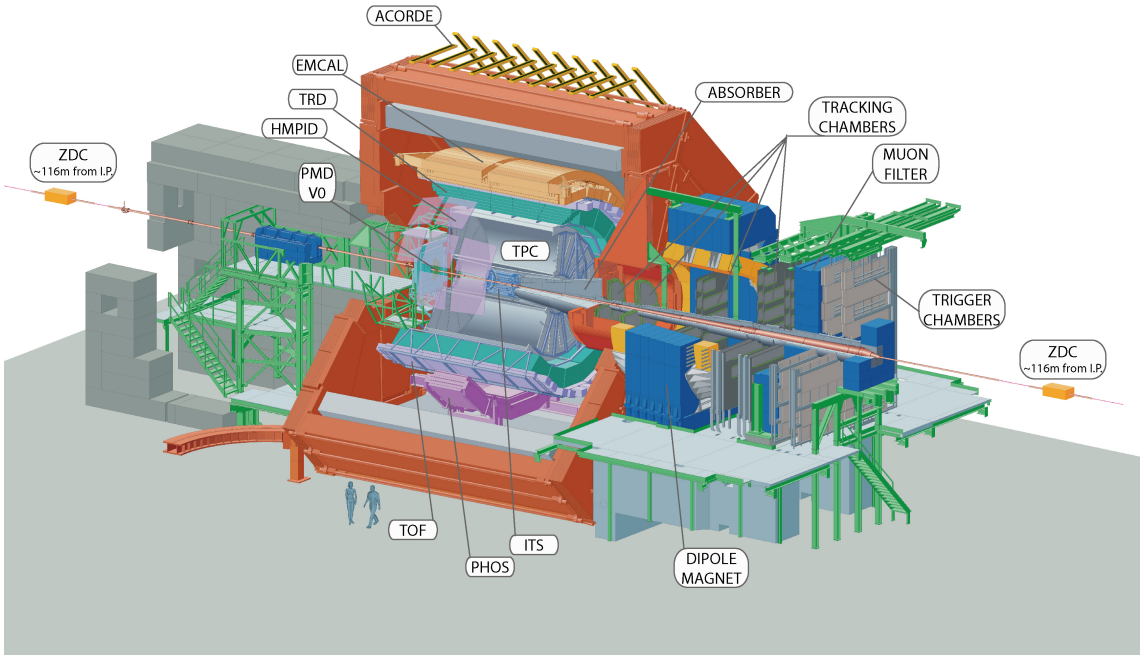

Figure 2.1.: Sketch of the ALICE Experiment

so-called central barrel is built inside the L3 magnet shown in red. The main detectors used in this analysis are the Time Projection Chamber (TPC), the Inner Tracking System (ITS) and the Time Of Flight (TOF) detector. They all provide full azimuthal[1] coverage, the positions and polar acceptances are summarized in tab. 2.2.
In the next sections I will shortly explain how these detectors work in principle and what they are used for in this analysis.

2.2.1. Inner Tracking System - ITS

The most inner detector in the experiment is the ITS. It is shown in fig. 2.2.
It consists of two layers of silicon pixel detectors (SPD) as the most inner layers, followed by two layers of silicon strip detectors (SSD) and two layers of silicon drift detectors (SDD). This detector setup provides excellent tracking and vertex reconstruction possibilities. In addition the pulse-height measurements from the four layers of the SSD and the SDD are

[1]The coordinate system used in ALICE is defined in A.3

Detector	Polar Acceptance	Position
SPD	$\|\eta\| < 2.0$	$r = 3.9$ cm
	$\|\eta\| < 1.5$	$r = 7.6$ cm
SDD	$\|\eta\| < 0.9$	$r = 15$ cm
	$\|\eta\| < 0.9$	$r = 23.9$ cm
SSD	$\|\eta\| < 1.0$	$r = 38$ cm
	$\|\eta\| < 1.0$	$r = 43$ cm
TPC	$\|\eta\| < 0.9$	$85 < r/\text{cm} < 247$
TOF	$\|\eta\| < 0.9$	$370 < r/\text{cm} < 399$

Table 2.2.: Position and polar coverage of detectors used in this analysis [ALI 14]

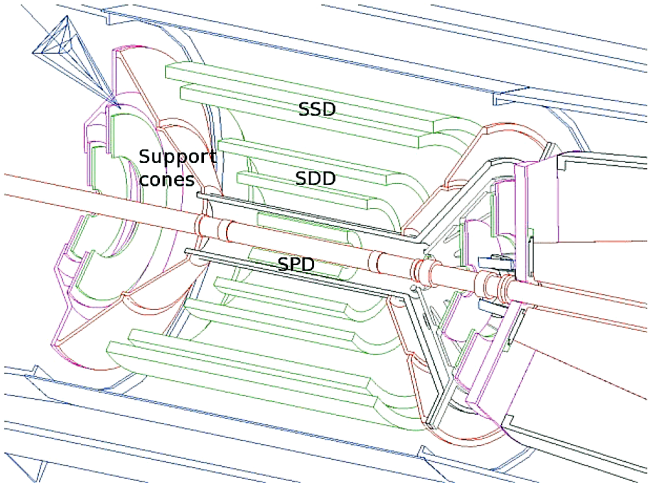

Figure 2.2.: Schematic sketch of the ITS with its support cones [BEO 12]

used for particle identification [ALI 99]. This is achieved via the particle's specific energy loss ($\mathrm{d}E/\mathrm{d}x$) in the active detector material and is shown for 2.76 TeV Pb–Pb collisions in fig. 2.3. The $\mathrm{d}E/\mathrm{d}x$ resolution is about 10% [JHS 16]. The black lines in the figure indicate the expected $\mathrm{d}E/\mathrm{d}x$ values for different particles. The clear separation of the different species at low momenta gives a possible handle on hadron rejection. In this analysis also the secondary vertex of decaying particles has to be reconstructed. The capability of this measurement is shown for Pb–Pb measurements and Monte Carlo simulations in fig. 2.4. We note the rather strong p_{T} dependence.

2.2.2. Time Projection Chamber - TPC

The ALICE TPC is shown in fig. 2.5. Its volume is about $90\mathrm{m}^3$ and filled with a mixture of Ne-CO_2 (90-10), Ne-CO_2-N_2 (90-10-5), Ar-CO_2 (88-12) in Run 1 and Run 2, respectively. Charged particles traversing the TPC will ionize the gas molecules and produce so-called primary electrons. An electric field between the central electrode and the endplates will

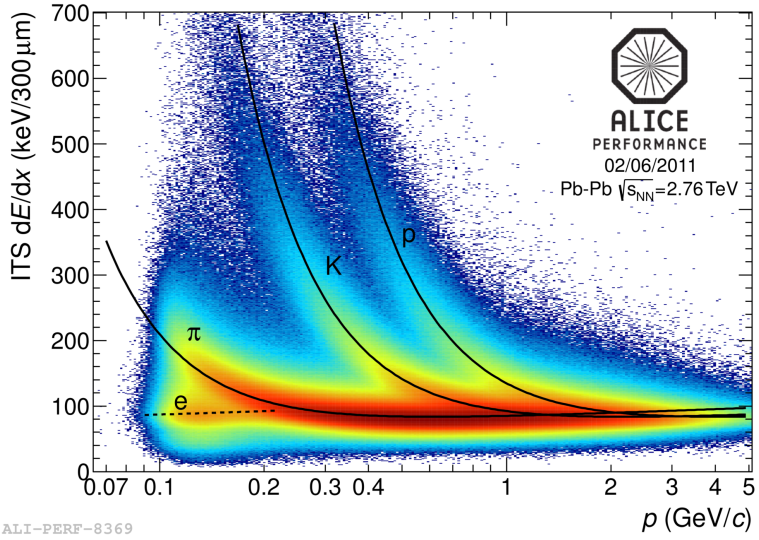

Figure 2.3.: dE/dx in the ITS for 2.76 TeV Pb-Pb collisions. The lines indicate the expected values from a Bethe-Bloch parametrization [JHS 16].

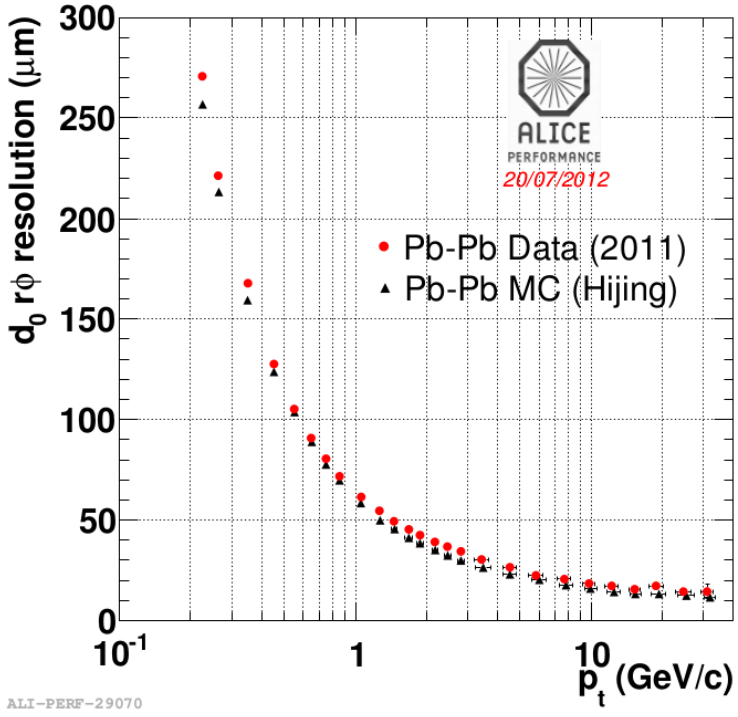

Figure 2.4.: Resolution of the distance of closest approach in the transverse plane versus p_{T} for current inner tracking system [ALI 12].

transport these electrons to the readout wire chambers (multi wire proportional chambers MWPC). In the ALICE experiment there are two different types of readout chambers: The inner readout chambers (IROC) and the outer readout chambers (OROC). They use

the same technology but have different size and slightly different wire geometry. The inner and outer field cages guarantee a constant field also in the boundary areas of the electric field. Due to multiple scattering with the gas molecules and the constant field the primary electrons drift with a constant velocity v_D towards the readout chambers.

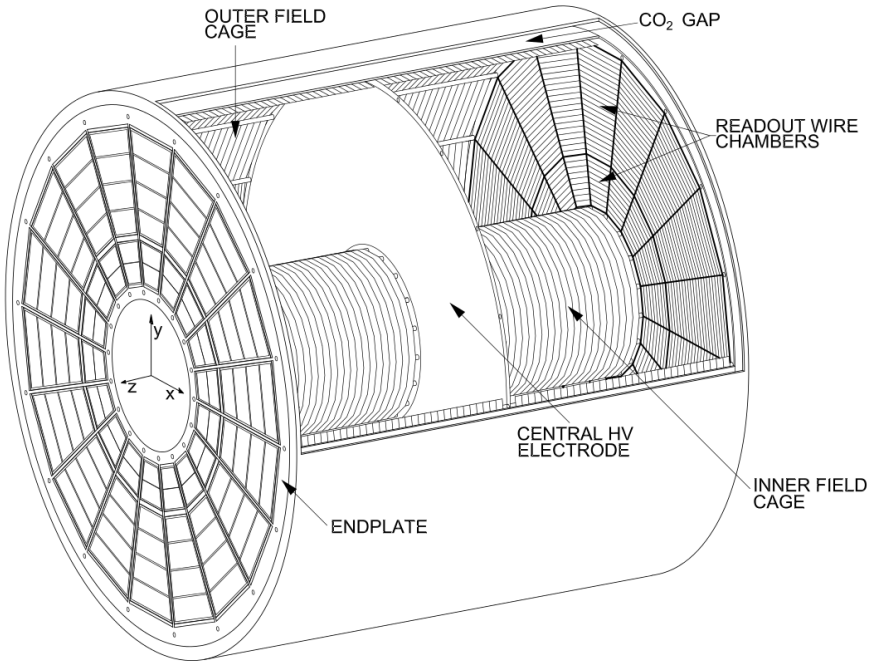

Figure 2.5.: Sketch of the ALICE TPC [LIP 11].

A schematic cross section of these is shown in fig 2.6 for the IROCs and OROCs.

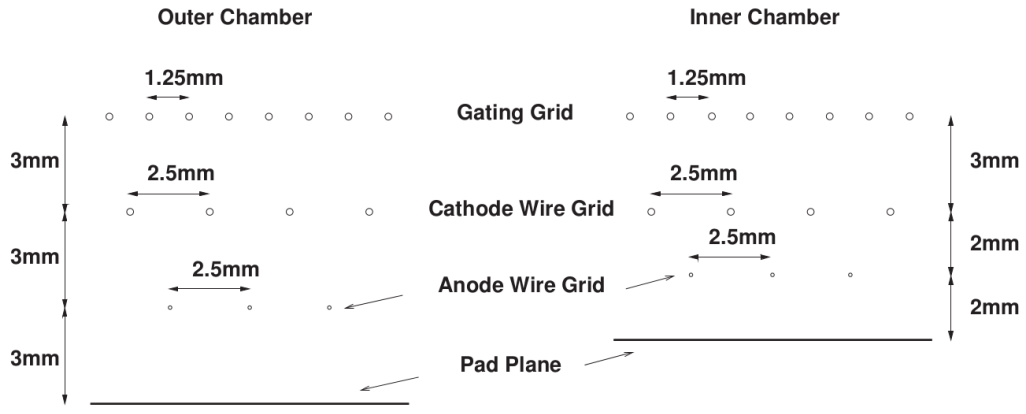

Figure 2.6.: Schematic cross section of the inner and outer readout chambers [ALM 10].

A primary electron entering the MWPC will drift to the anode wire plane. Due to the high voltage between the cathode and anode wires a gas amplification will start and electrons and ions will be produced in an avalanche near the anode wire. The highly mobile electrons

are quickly absorbed by the anode wire, resulting in a positive space charge by the ions around the anode wire. This space charge then induces a mirror charge in the pads, which can be measured. The backdrifting ions are then absorbed by the gating grid so they do not end up in the drift volume where they would distort the driftlines of the primary electrons. With the information of the pad position, timing information of the TPC cluster, and the knowledge of the electron drift velocity in the TPC gas it now is possible to reconstruct tracks in the TPC in 3 dimensions. Due to the magnetic field from the L3 magnet of 0.5 T its is also possible to calculate the momentum of the track from its curvature.
In addition the TPC can measure the specific energy loss $\mathrm{d}E/\mathrm{d}x$ of each particle via the amount of charge deposited by the track on the pads. The $\mathrm{d}E/\mathrm{d}x$ for a charged particle traversing a medium is given by the Bethe-Bloch formula

$$\frac{\mathrm{d}E}{\mathrm{d}x} = \frac{4\pi N e^4}{m_\mathrm{e} c^2 \beta^2} z^2 \left(\ln \frac{2 m_\mathrm{e} c^2 \beta^2 \gamma^2}{I} - \beta^2 - \frac{\delta(\beta)}{2} \right). \tag{2.1}$$

In this equation $m_\mathrm{e}c^2$ is the electron rest mass, N the electron number density, z the charge of the traveling particle, β its velocity and $\gamma^2 = 1/(1-\beta^2)$. The material dependent mean excitation energy is denoted by I. The δ is a term introduced by E. Fermi to take medium polarization into account [BRR 10]. This equation holds true for charged particles with a $\beta\gamma$ from 0.1 to several hundred. For gamma values of about 1000 and higher, radiative energy loss becomes important. In the observed momentum regime by the ALICE experiment of $0.1 < p < 100$ GeV/c, the Bethe-Bloch parametrization is valid for all particles except electrons. In the ALICE experiment a parametrization of the Bethe-Bloch equation is used that was introduced by the ALEPH collaboration and is given in eq. 2.2 [ALI 14]:

$$f(\beta\gamma) = \frac{P_1}{\beta^{P_4}} \left(P_2 - \beta^{P_4} - \ln(P_3 + \frac{1}{(\beta\gamma)^{P_5}} \right). \tag{2.2}$$

Here β and γ are the same variables as in eq. 2.1 and $P_1 - P_5$ are fit parameters. As one can see in the parametrization as well as eq 2.1 the specific energy loss depends only on $\beta\gamma$. In fig 2.7 the specific energy loss is plotted vs the momentum. We can see that the contributions from the single particle species are not on top of each other and ordered by mass. The electrons appear as a flat contribution since their minimum would be at much lower momentum.

2.2.3. Time Of Flight - TOF

The ALICE TOF system uses multigap resistive plate chambers (MRPCs). They consist of a stack of glass plates with gas-filled gaps. An external field is applied, so a traversing charged particle will start an avalanche in the gaps. This avalanche is stopped by the glass

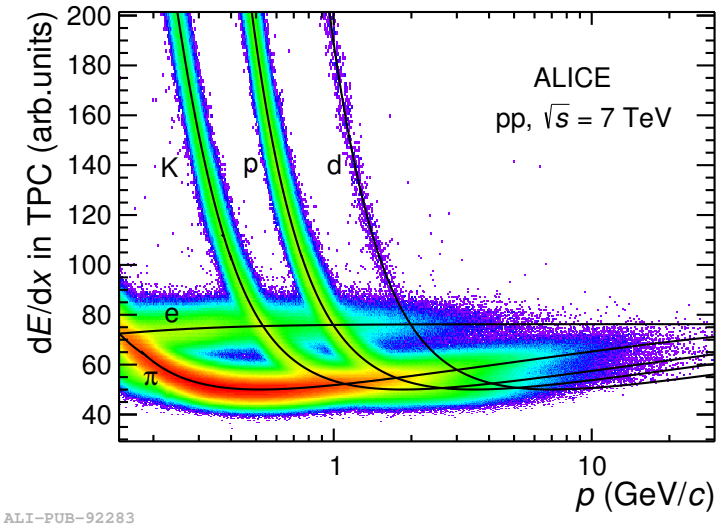

Figure 2.7.: Distribution of $\mathrm{d}E/\mathrm{d}x$ as a function of p measured in the TPC for $|\eta| < 0.9$. The continuous curves represent the Bethe-Bloch parametrizations for different particle species. [ALI 15]

plates. However a signal is induced in the pickup electrodes. The matching efficiency of the TOF signal with reconstructed tracks is shown in fig. 2.8. Here we can see the matching

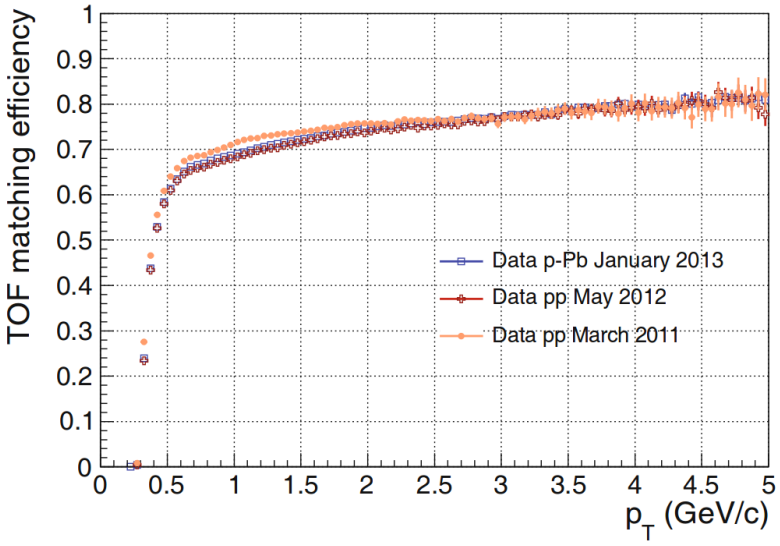

Figure 2.8.: Track matching efficiencies of the TOF signal vs. p_{T} for different datasets [AKI 13].

efficiency for different collision systems and periods.

Taking the formula $p_T = 0.3 \cdot B \cdot \rho$ GeV/(c T m), where p_T is the transverse momentum, B is the magnetic field, and ρ is the bending radius of the track together with the substitution

$R = 2\rho$, where R is the most outward radial position the track reaches, it can easily be seen that - given the standard magnetic field of 0.5 T in ALICE - primary charged tracks with $p_T < 0.3$ GeV/c cannot reach the TOF detector located at a radial position of 3.7 m away from the primary vertex. Consequently, the TOF matching efficiency is zero for such small momenta. For $p_{\mathrm{T}} > 0.3$ GeV/c the matching efficiency rises steeply and starts to saturate at 0.5 GeV/c. The further improvement at higher p_T results from the better knowledge of the spatial position of the track. In the limit of infinite transverse momentum, the track model reduces to a straight line fit. The timing information from the TOF measurement can be correlated with the start time given by the T0 detector or, if enough tracks hit the TOF also by the TOF itself.
The latter method allows to extract the intrinsic timing resolution in the limit of a large number of tracks ($N_{\mathrm{Track}} \geq 20-30$) reaching the TOF to be about 80 ps. The performance slightly deteriorates to 100 ps for 5 contributing tracks. The event time determination by the TOF detector itself becomes particularly useful in pp collisions where due to limited acceptance, the T0 detector cannot provide the event time. The TOF algorithm provides an independent means of determining the start time with an efficiency better than 90% for at least 5 tracks reaching the TOF detector [AKI 13]. The measured arrival time together with the traveled path length from the track model allows to determine the particle's velocity. The resulting PID capabilities are depicted in fig. 2.9. The figure shows clearly

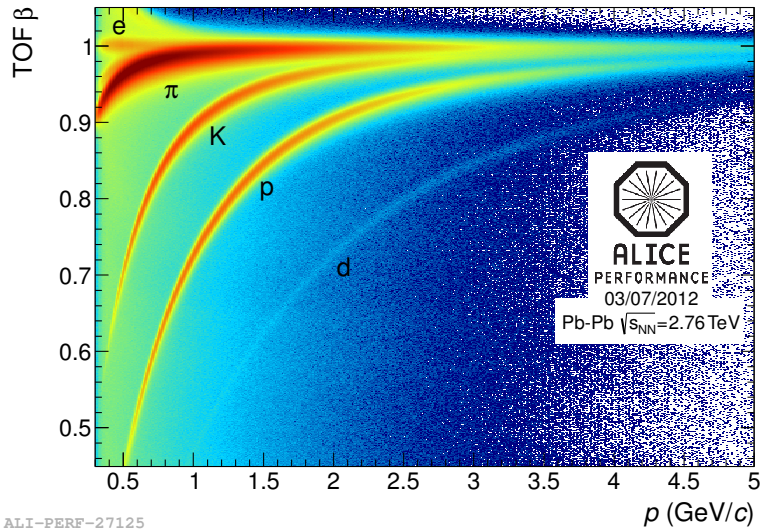

Figure 2.9.: Momentum dependence of the particle velocity [PRE 12].

the possibility for particle identification, especially in the lower to intermediate momentum region. But also for higher momentum the TOF provides a good separation of hadrons.

3. Analysis

The analysis performed in this thesis is a pair analysis. It follows some specific steps to get from a sample of single tracks to a pair spectrum. I will shortly summarize the main steps now and explain them in detail in the remainder of this chapter.
The first step is to select tracks from the data sample. The criteria we apply for the selection should make sure that we end up with a set of high-quality tracks of electrons and positrons. These can then be used to build pair spectra from which the signal is calculated. This process is explained in detail in [PHE 15].

3.1. Dataset and Monte Carlo

3.1.1. Dataset

This analysis was done in proton-proton collisions at a center of mass energy $\sqrt{s} = 7$ TeV taken with ALICE at the LHC at CERN in 2010. The dataset is a minimum-bias dataset with approximately 400 million events used for physics analysis.
Uninterrupted intervals of data taking are called runs. These runs can show different behaviour concerning the detector performance. The ALICE monitoring system is able to select runs on the basis of certain quality criteria. The best runs to do physics analysis on are flagged in the so-called 'run condition table' with a quality of 1. For this analysis only runs with this quality were used. A list of the used runs is given in A.4.

3.1.2. Monte Carlo Production

As simulations we used three different Monte-Carlo productions. This is necessary since the minimum-bias production LHC14j4 does not contain enough statistics of heavy-flavour particles. Therefore one MC production with enhancement of B- and D-Mesons and one with enhancement of J/ψ were used in addition. All MC productions are anchored to the pass4 reconstruction of the 2010 pp dataset to model all effects concerning detector performance correctly. The simulations are all generated in PYTHIA6 and propagated through the detector by GEANT3. The only difference is that the minimum bias and the J/ψ MC used the Perugia2011 tune, the heavy-flavour MC used the Perugia0 tune. This should not make any difference in this analysis, since it only concerns the hadronization parameters in the MC. This is corrected for in the later analysis steps.

3.1.3. Track Selection

The tracks used for the analysis where selected using cuts on the single tracks. The cuts are summarized below:

- $p_{\mathrm{T}} > 0.4$ GeV/c
- $-0.8 < \eta < 0.8$
- no *kinks*
- ITS
  - ITS *refit* required
  - at least 4 cluster
  - hit in the first layer
- TPC
  - TPC *refit* required
  - at least 100 pad rows crossed
  - at least 80 cluster for $\mathrm{d}E/\mathrm{d}x$ measurement
  - less than 10% *s*hared clusters
  - $\frac{\mathrm{crossedrows}}{\mathrm{findableTPCcluster}} > 0.5$
  - χ^2 per TPC cluster belonging to a track ≤ 3

The requirement of a certain minimal amount of associated clusters in general ensures a good measurement of the track. On the one hand of the trajectory because we have more space points for the track reconstruction. On the other hand a cluster also is a measurement of the specific energy loss $\mathrm{d}E/\mathrm{d}x$ we use for particle identification in the TPC and ITS. Demanding a hit in the first layer of the ITS is a very powerful method to reject conversions. The only conversions left should then stem from conversion in the beam pipe. There also is a small chance, that the conversion happens in the active layer of the first ITS layer and produces a hit there or a cluster is wrongly assigned to a track from a conversion which would leave conversions in the final track sample. These contributions can be efficiently rejected by imposing specific pair selection criteria discussed in section 3.3.1.

3.2. Particle Identification

For electron identification we mainly use the $\mathrm{d}E/\mathrm{d}x$ of the particle in the TPC. Also the signal from the energy loss in the ITS is used as well as the time-of-flight measurement.

The main background in an electron measurement are pions. Electrons are selected and pions and other hadronic contaminations are rejected combining different detector signals. This is done by cutting into the so called numbers of sigma nσ distributions and not the measured detector signal directly. The $n\sigma$ is calculated as eq. 3.1.

$$n\sigma = \frac{\text{signal}_{\text{track}} - \text{signal}_{\text{expected}}}{\sigma_{\text{track}}} \tag{3.1}$$

The signal of the track here is the measured signal from the detector. We then subtract the expected value for a certain particle species at the measured momentum and divide it by the resolution σ. So the nσ tells us how far away from the expected value for a certain particle species the measurement is while taking the resolution of the dE/dx measurement into account.

3.2.1. Electron Selection

In this section I will concentrate on the particle and electron identification possibilities of the detectors explained in sec. 2.2 and how they are used in this analysis.

3.2.1.1. ITS

Besides tracking capabilities the ITS is also used for hadron rejection.
In fig. 3.1 $n\sigma_{\text{e}}^{\text{ITS}}$, as calculated with 3.2, is shown as a function of momentum.

$$n\sigma_{\text{e}}^{\text{ITS}} = \frac{\langle dE/dx \rangle_{\text{ITS}} - dE/dx_{\text{expected}}}{\sigma_{\text{track}}} \tag{3.2}$$

The solid line shows the expected value for electrons, the dashed lines indicate the selection interval for electron candidates. We select electrons in an interval from -3 $< n\sigma_{\text{e}}^{\text{ITS}} <$ 1. This way we reject mainly kaons and protons at momenta of up to 2 GeV/c.

3.2.1.2. TOF

The time-of-flight measurement is shown in fig. 3.2. Tracks are selected if they fulfil the requirement of -3 $< n\sigma_{\text{e}}^{\text{TOF}} <$ 3. Tracks with no TOF signal are not excluded due to the finite track matching efficiency. When a TOF signal is present we can see a good discrimination for kaons up to 2 GeV/c and protons over the whole momentum range. Also the separation of electrons and pions at lower momentum than 500 MeV/c can be seen.

3.2.1.3. TPC

Looking into fig. 3.1 and fig. 3.2 we can see that there are a lot of pions left after imposing the selection criteria on the ITS and TOF information. In fig. 3.3 the TPC measurement

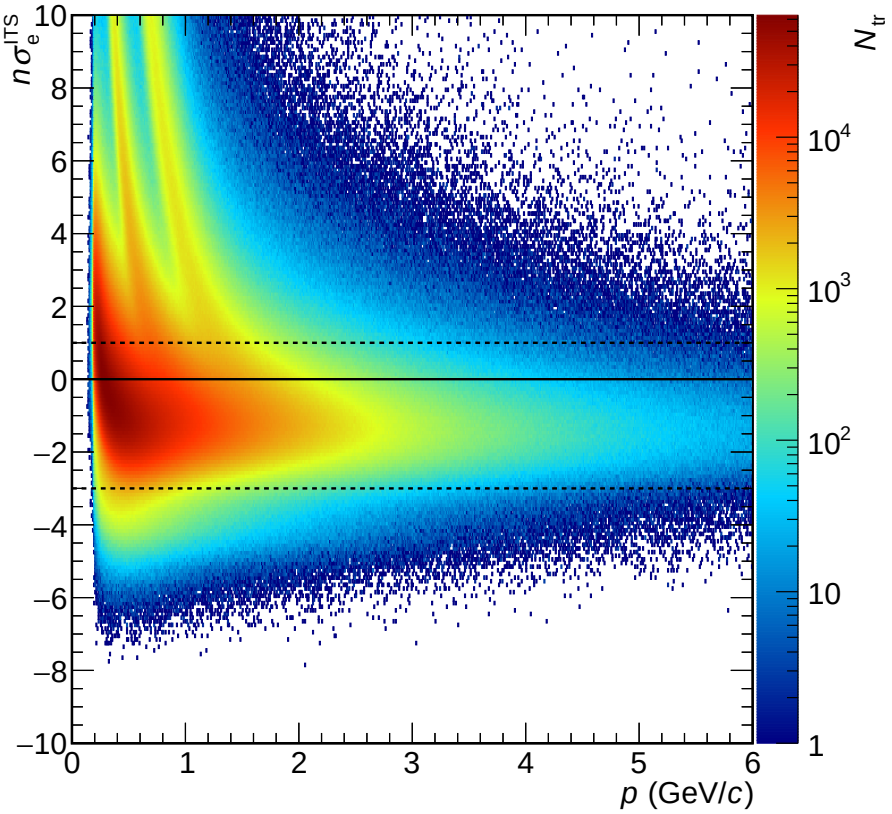

Figure 3.1.: dE/dx measured in the ITS. The solid line indicates the expected value for electrons where the dashed lines show the cut criterion.

is shown before and after the cuts in the ITS and TOF. The signal here is calculated with eq. 3.2 using the mean energy loss from the TPC measurement. We can clearly perceive the hadron rejection capabilities of the ITS and TOF criteria. Also we can see a clearer separation of the electrons from the pions. In the TPC we use two different cuts. On the one hand we use an electron inclusion cut of -1.5 $< n\sigma_{\mathrm{e}}^{\mathrm{TPC}} <$ 4 as indicated by the dashed lines in fig. 3.3. In addition a pion rejection cut of -100 $< n\sigma_{\pi}^{\mathrm{TPC}} <$ 3.5 is used to exclude most pions. Here, not the expected value for the electron but the pion is taken to calculate $n\sigma_{\pi}^{\mathrm{TPC}}$. The final tracks selected for analysis are shown in fig. 3.4. Here we can still see a small contamination from kaons and protons. These are no further concern since we are looking into correlated pairs in the end. The possibility to get a correlated pair from hadrons is negligibly small.

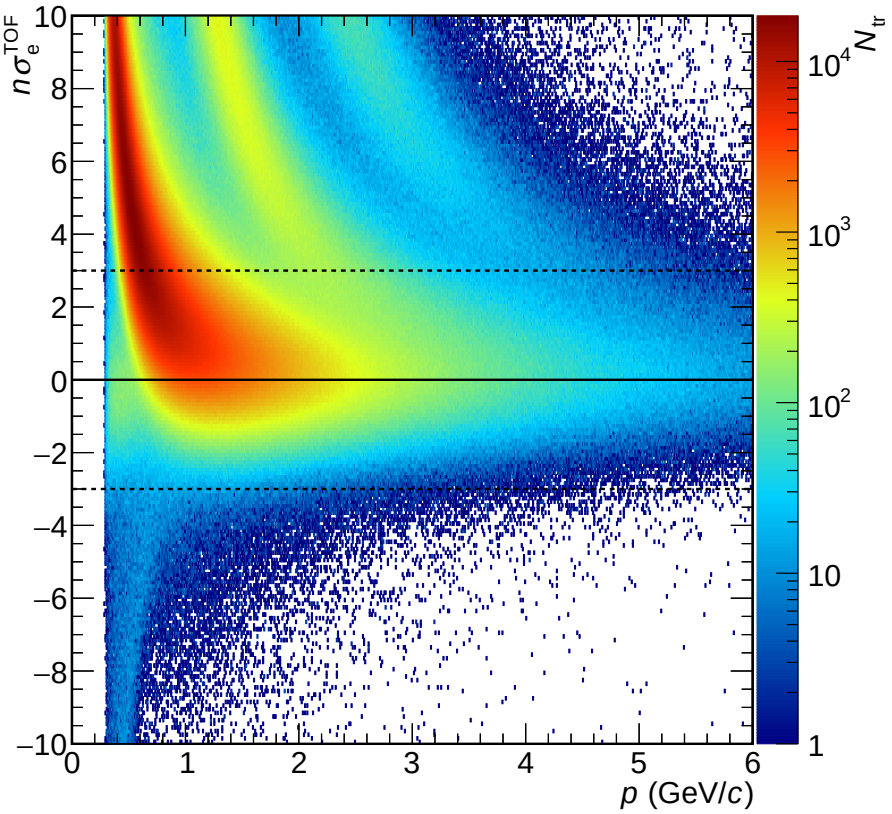

Figure 3.2.: Number of tracks as a function of momentum and $n\sigma_e^{TOF}$.

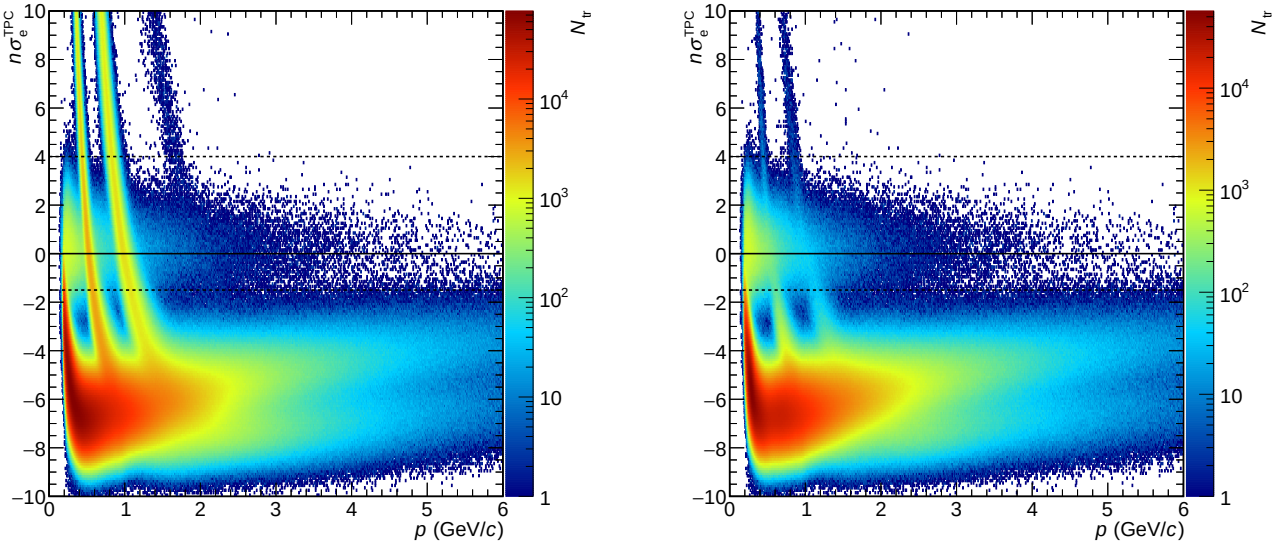

Figure 3.3.: Number of track as a function of momentum and $n\sigma_\pi^{TPC}$. On the left before any particle identification cuts, on the right after the TOF and ITS cuts.

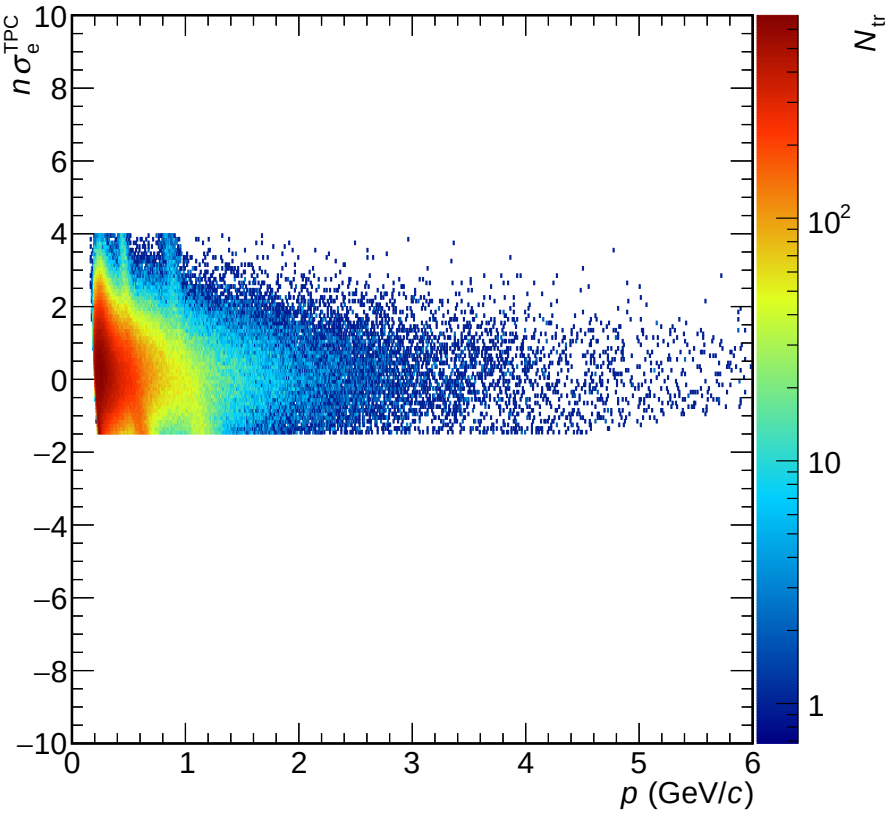

Figure 3.4.: $\mathrm{d}E/\mathrm{d}x$ of tracks selected for analysis in the TPC.

3.3. Pairing of Electron Candidates

In this analysis the signal is composed of dielectrons from $J^{PC} = 1^{--}$ resonances, other electromagnetically decaying mesons, dielectrons from virtual direct photons, as well as the contribution from initial Drell-Yan annihilation. The so called background is mainly conversions of photons in the material of the beam pipe. To extract the signal from the single measured electrons and positrons we use a pairing technique which will be explained in the next section.

3.3.1. Pair Spectra

For the calculation of the signal we take all electron candidates that are essentially all tracks that survive the track cuts in sec. 3.2. From these we form different pair spectra:

- Same-event unlike sign: Every electron is paired with every positron in the same event
- Same-event like sign: Electrons are paired with electrons, positrons with positrons in the same event
- Mixed-event unlike sign: All electrons are paired with positrons from a different event.
- Mixed-event like sign: All electrons are paired with electrons from different events, positrons likewise.

The same-event unlike-sign spectrum contains the signal we want to measure illustrated in fig. 3.5, as well as combinatorial and correlated background as sketched in fig. 3.6. These are described by the sum of the two same-event like-sign spectra. Another method to describe the background would be to use the mixed-event spectra and fit them in a region where we only expect background. The problem with this is, that since we measure a dielectron continuum there is no region where this can easily be done. Also the mixed event spectra do not describe correlated background like double Dalitz decays from π^0 or particles from jets shown on the right in fig 3.6. Therefore, the background is estimated via the like-sign spectrum.

3.3.1.1. Prefilter track cuts

In this analysis an additional prefilter was used. The reason to introduce prefilter cuts is that it might happen, that a conversion or a Dalitz decay produces one leg that will survive the normal track selection and one soft leg that will not. The surviving leg will then only contribute to the combinatorial background during the pairing step. The idea of a prefilter is to create a set of tracks with very loose restrictions, so as many of the

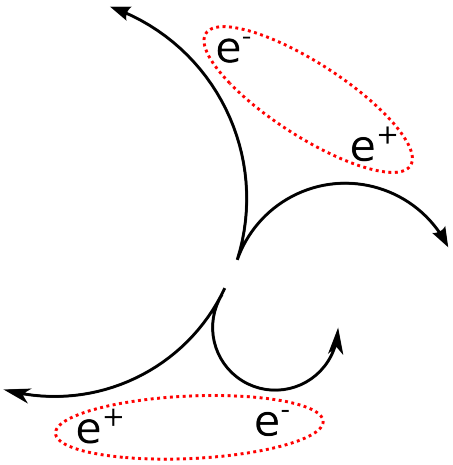

Figure 3.5.: Schematic drawing of different ways to construct an unlike sign pair. In red the real signal is marked

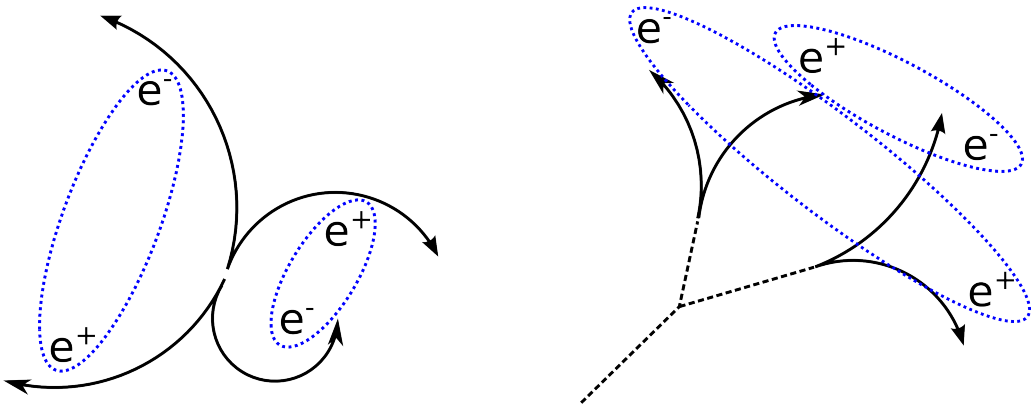

Figure 3.6.: Schematic drawing of electrons and positrons from decays on the left the combinatorial background is marked, on the right the correlated background is marked.

Dalitz pairs and conversion pairs end up in this sample with both their legs. The used track cuts are shown below:

- $0.08 < p_{\mathrm{T}} < 100$ GeV/c
- $-1.1 < \eta < 1.1$
- no *kinks*
- ITS
  - ITS *refit* requiered
  - at least 3 clusters
  - hit in the first or second ITS layer

After pairing, a cut on the opening angle to be larger than 50 mrad is applied. Like this the tracks that would only contribute to the combinatorial background can be rejected. The like-sign and unlike-sign spectra with and without the used prefilter are shown in fig 3.7. We can see, that in the mass range of 500 MeV/c^2 to 2 GeV/c^2 the relative separation of

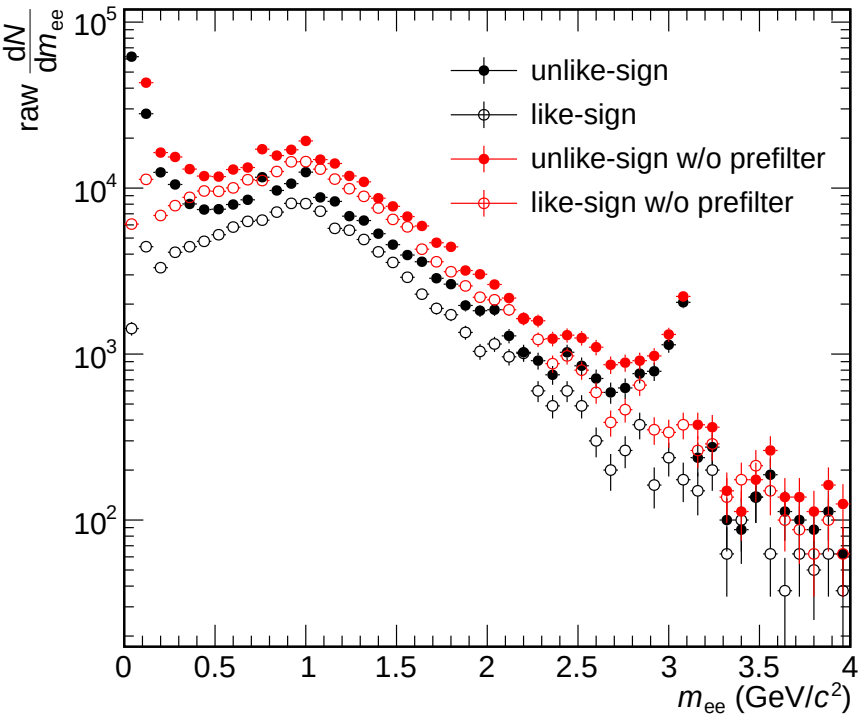

Figure 3.7.: Like-sign and unlike-sign spectra with and without prefilter.

unlike-sign and like-sign becomes larger, which is due to the reduction of the combinatorial background. This can also be seen looking into the signal-to-background ratio in fig 3.8. It is apparent, that the signal to background ratio increases over the whole mass range when using the prefilter although for the significance, as shown in fig. 3.9, no drastic change is observed.

3.3.2. Signal Extraction

To obtain the signal we will subtract the like-sign from the unlike-sign spectrum. The normalization of the same-event like-sign spectrum is intrinsically correct and we do not need to fit it to the unlike-sign spectrum or normalize otherwise. The only problem is that the detector has different acceptances for like-sign and unlike-sign pairs at low invariant

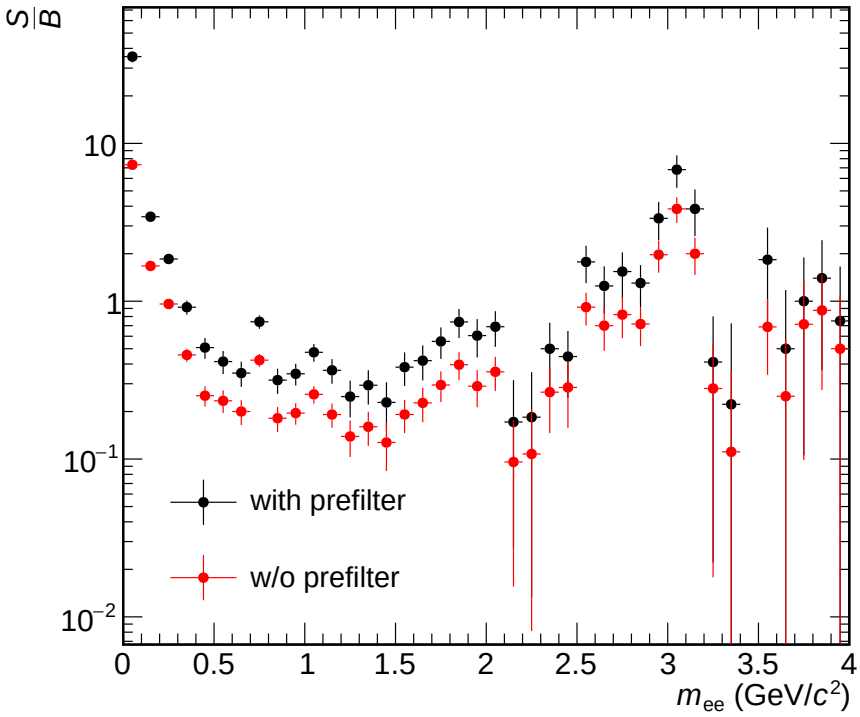

Figure 3.8.: Signal to background ratio with and without prefilter.

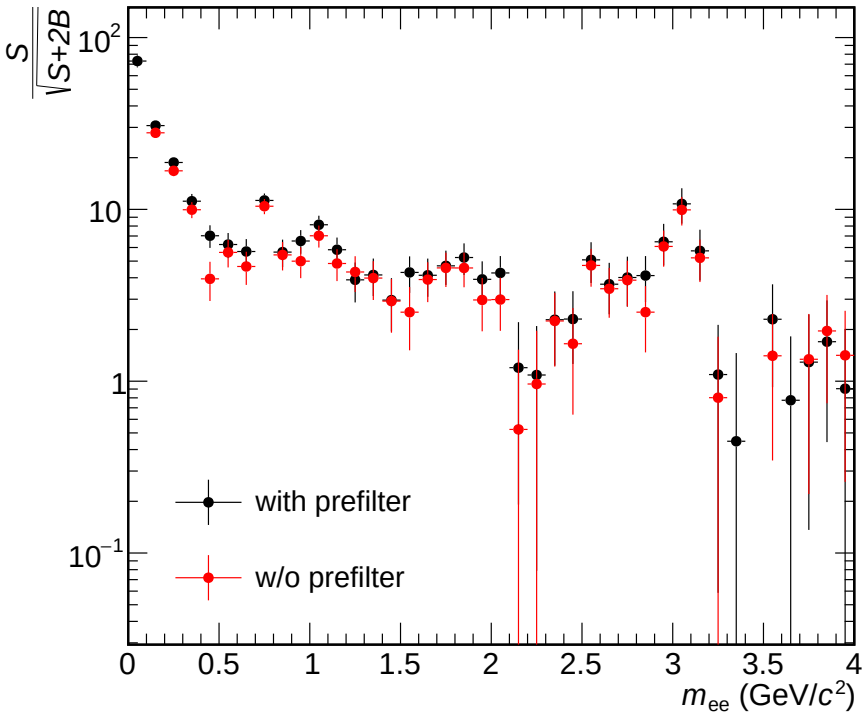

Figure 3.9.: Significance with and without prefilter.

masses. This is corrected for by the so-called R-factor, which is determined from the

mixed event spectra. The formula for the signal calculation is then given by eq. 3.3. In this analysis the R-factor is applied for masses smaller than 500 MeV/c^2.

$$\text{Signal} = ULS_{\text{SE}} - R \cdot LS_{\text{SE}} \tag{3.3}$$

$$R = \frac{LS_{\text{mix}}}{ULS_{\text{mix}}} \tag{3.4}$$

The final invariant mass spectrum is shown and compared with the hadronic cocktail calculations in fig. 3.10.

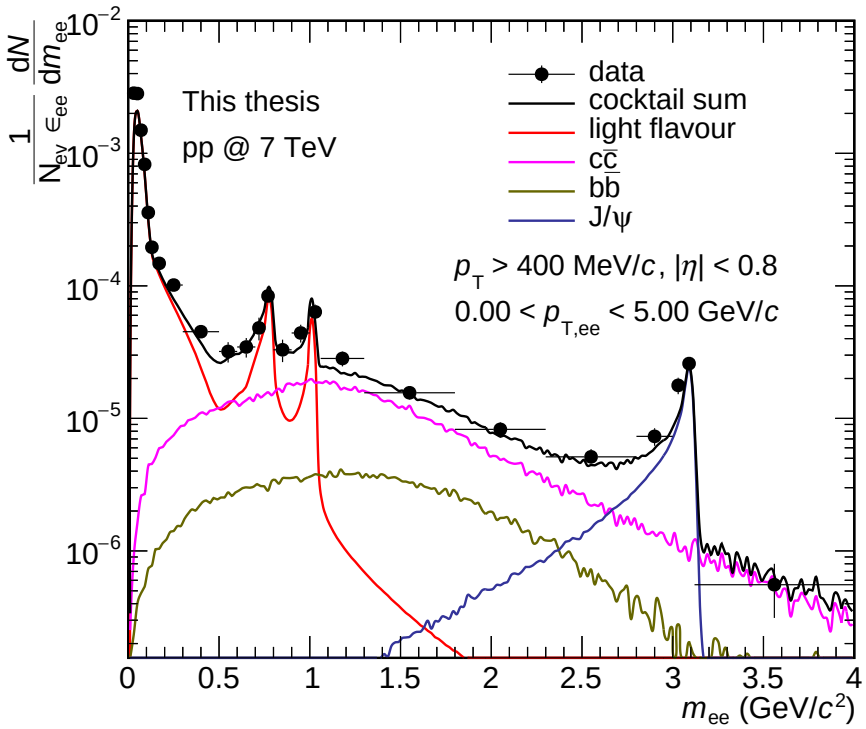

Figure 3.10.: Invariant mass spectrum of dielectrons from pp collisions at $\sqrt{s} = 7$ TeV compared to the hadronic cocktail estimations.

4. Template Distributions from Monte Carlo

As we see in fig. 3.10 the mass region behind the ϕ is strongly dominated by the contribution from $c\bar{c}$ production in the hard scattering processes. In this region we expect a contribution of thermal radiation from the early stage of the collision. A measurement can hardly be done by looking into the mass spectrum since the mass distributions of thermal radiation and open heavy-flavour dielectrons are very similar [ALI 12]. Separating both contributions can be achieved by exploiting the decay kinematics as discussed in chapter 1.5. In this chapter we explain the construction of DCA_{ee}-templates for the expected sources in the dielectron continuum. The constructed templates are then normalized with realistic abundances from hadronic cocktail calculations. Finally, the measured signal is compared to Monte-Carlo calculations to unfold different sources contributing to the dielectron spectrum.
As will be shown in the following, our applied procedure allows to experimentally separate the contribution from heavy-flavour decay electrons and the electromagnetic radiation from the QGP.

4.1. Template Construction

To construct templates for this analysis we used the MC information to select dielectrons. For the decaying pions or J/ψ this gives a correct description of the DCA_{ee} since the dielectron is identified unambiguously via the MC information. For the semi-leptonic decays of B- and D-Mesons it is more complicated, since the electron and positron do not stem from the same particle. In the following sections we will explain how to obtain templates for the different particle species we expect. We extracted inclusive templates for dielectrons from decays of B- and D-mesons, templates for the decays of direct J/ψ and feed down from B-mesons decaying into J/ψ as well as the Dalitz decays of neutral pions into a dielectron. The pion template was then used to describe the shape of all light-flavour prompt contributions in the DCA_{ee} spectra.

4.1.1. π^0-Mesons

The π^0 mass region is considered from 80 MeV/c^2 to 140 MeV/c^2. We start with this large mass to be sure to have as few as possible conversions left in the sample. The DCA_{ee} spectra for two $p_{T,ee}$ intervals are shown in fig. 4.1. Both distributions agree with

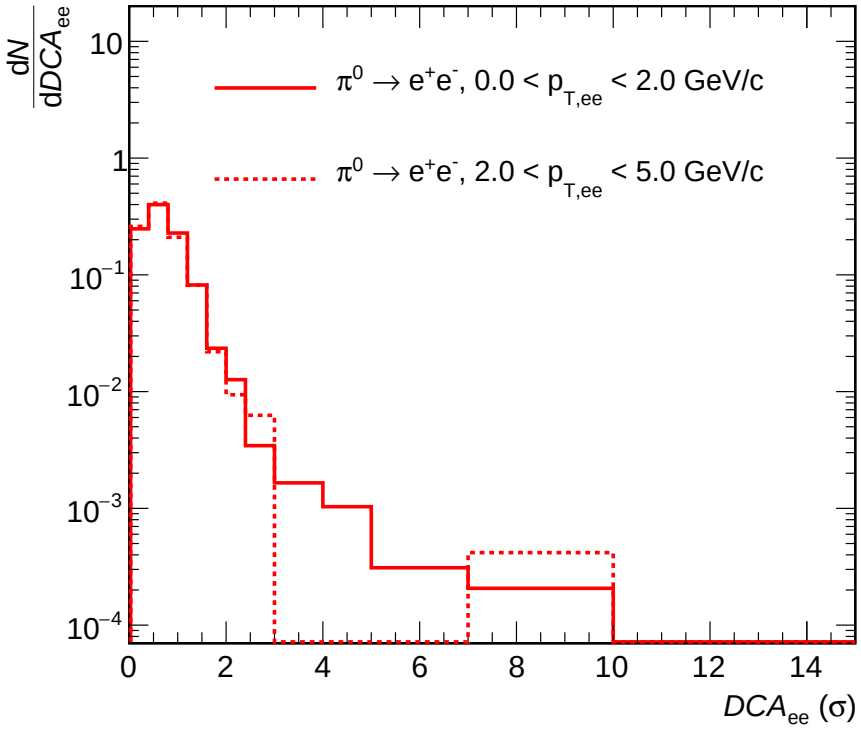

Figure 4.1.: DCA_{ee} spectrum of π^0 Dalitz decays in two different $p_{\mathrm{T,ee}}$ intervals. All spectra are normalized to unity for better comparison.

each other under consideration of the statistical uncertainties. From this we conclude, that there is no $p_{\mathrm{T,ee}}$ dependence for the π^0 Dalitz decays in terms of DCA_{ee}. This is expected, since DCA_{ee} should by construction be sensitive to the decay length of a mother particle. The π^0 decays directly at the vertex no matter what momentum it has. This leads to both tracks of the pair pointing towards the vertex and a spectrum with a maximum at small DCA_{ee} which is steeply falling. We take the contribution from these decays as an approximation for all prompt light-flavour decays into dielectrons.

4.1.2. J/ψ-Mesons

For the template of directly produced J/ψ we used the MC information and set two conditions, the first is, that a J/ψ decayed into a dielectron, the second one, that there is no B-meson in the decay history of the J/ψ. For the feed-down from B-meson decays the second condition is then changed, so the J/ψ really came from a decaying B-meson. Both spectra are shown for two different $p_{\mathrm{T,ee}}$ intervals in fig. 4.2.

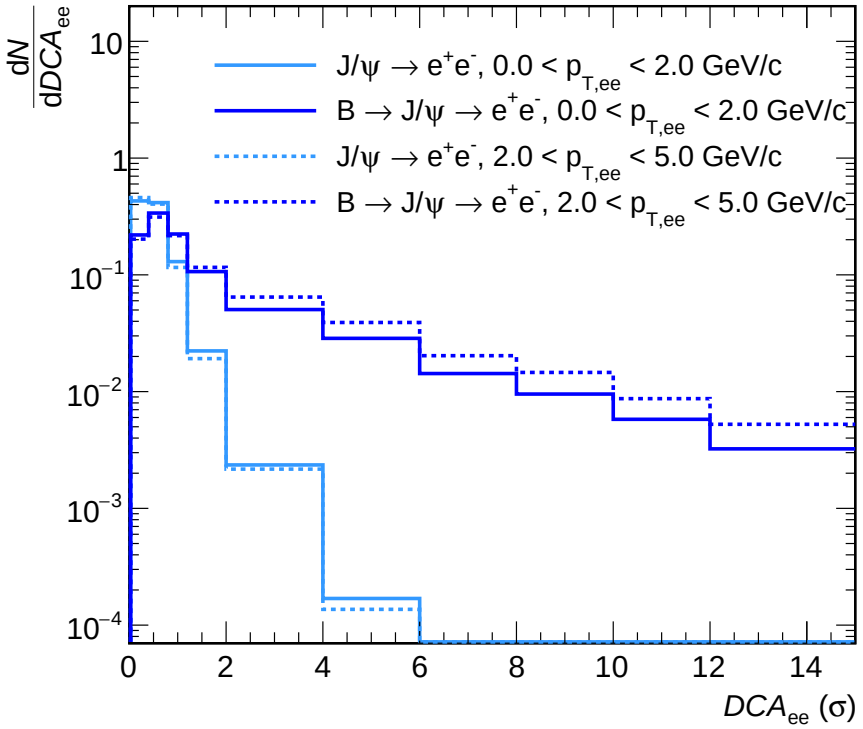

Figure 4.2.: DCA_{ee} spectra for prompt J/ψ decaying into a dielectron and feed-down from B-mesons decaying into J/ψ, then decaying into a dielectron both in two different p_{T}intervals.

Here we can nicely see the difference in the DCA_{ee} spectra between a dielectron from a decay at the primary vertex (prompt J/ψ) and and a non-prompt contribution. The prompt part has its maximum at low DCA_{ee} and then falls very steeply similar to the π^0 spectrum. The non-prompt also has a maximum at low DCA_{ee}, but then gives a way harder spectrum since more particles decay away from the main interaction point.
We can also see that there is no $p_{\mathrm{T,ee}}$ dependence for the prompt J/ψ whereas for the non-promt J/ψ the higher $p_{\mathrm{T,ee}}$ interval gives a harder spectrum. For the prompt J/ψ the same argument as for the π^0 holds true. The non-prompt J/ψ on the other hand will fly away from the vertex and after some time decay. The distance it travels is correlated with the momentum it has and thus with its p_{T}. If its momentum is larger, the distance gets larger and consequently results in a harder DCA_{ee} spectrum.

4.1.3. D-Mesons

There are two different types of open-charm mesons: The charged and the neutral D-mesons. The main difference between the two is the branching ratio for semi-leptonic decays into electrons and the rather large difference in their decay length shown in tab. 4.1.

	B.R.: $e^{\pm}$ semi-leptonic	decay length $c\tau$
$D^0\bar{D}^0$	$(6.49 \pm 0.11)\%$	122.9 μm
$D^{\pm}$	$(16.07 \pm 0.30)\%$	311.8 μm

Table 4.1.: D-meson branching ratio to electrons and decay length [CPC 14].

Now there are two things we have to take into account when constructing a template for the D-mesons. On the one hand we have to assume, that the DCA_{ee} spectra for charged and neutral D-mesons are different, since their decay lengths are not the same. On the other hand the enhancement of heavy flavour in the MC will not give us the correct ratio of charged and neutral D-mesons since some of the decays have been forced to get more statistics.
The procedure to get a correct description of the DCA_{ee} spectrum for open charm mesons is the following:

- obtain templates for charged and neutral D-mesons separately from MC
- add the two templates considering the different branching ratios as weights

For the first step we used the MC information to select electrons and positrons that result from decays of charged or neutral D-mesons and make sure that these D-mesons are no decay products of beauty mesons. The selected electrons and positrons are then used to form an unlike-sign pair spectrum. The two different unlike-sign spectra then are added up to the inclusive spectrum with a weighting factor

$$\frac{D^{\pm}D^{\mp} \to e^+e^-}{D^0\bar{D}^0 \to e^+e^-} = \frac{\text{B.R.}(D^{\pm} \to e^{\pm})^2}{\text{B.R.}(D^0 \to e^{\pm})^2} = \frac{16.07^2}{6.49^2} = 6.13. \tag{4.1}$$

Here we only took the the unlike-sign spectra instead of calculating the signal. This is possible under the assumption, that the signal and unlike-sign spectrum have the same shape. Since we only add the DCA of the single tracks we do not take the angle into account. This means DCA_{ee} is only a scalar quantity, not a vectorial, thus it should not matter if the electron and positron are from correlated D-mesons or not. The result of this is shown in fig. 4.3.
The figure evidently exhibits that the observable DCA_{ee} is sensitive to the finite decay length of the D-mesons. In comparison to the prompt sources we can already see the

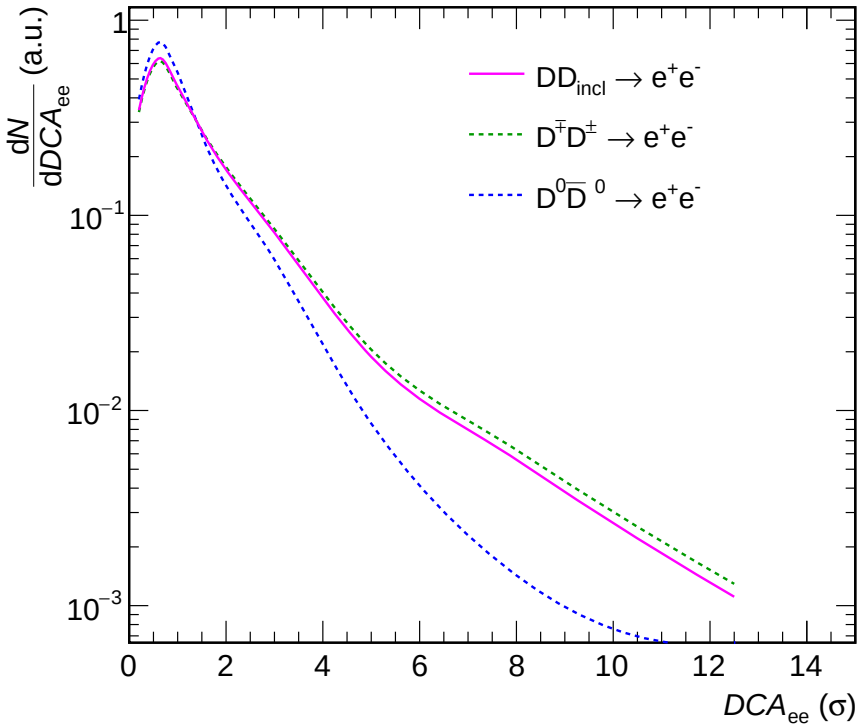

Figure 4.3.: Templates for DCA_{ee} spectra of dielectrons from charged, neutral and inclusive D-mesons in MC.

harder spectrum of the D-mesons and that it is dominated by the charged D-mesons. The next step is to check the pair transverse momentum dependence of the spectrum. It is shown for two different intervals in fig. 4.3. Here we can see, that the DCA_{ee} is no function of the $p_{T,ee}$ as far as D-mesons are concerned.

4.1.4. B-Mesons

For the B-mesons the case is more complicated than for the D-mesons. The problem is not the difference in decay length for charged and neutral B-mesons but in the decay channels for B-mesons into electrons. The main decay channels are shown in Tab. 4.2. From these decay modes we now can calculate the branching ratios for dielectrons. With B-mesons there is the possibility of oscillation of $B \rightarrow \bar{B}$. This leads to real signal ending up in the like-sign distribution. If the signal then is calculated there is already the oscillation part missing and since we then subtract the like-sign distribution the signal will be missing the part from oscillation twice. We can not get around this in data, so we have to do

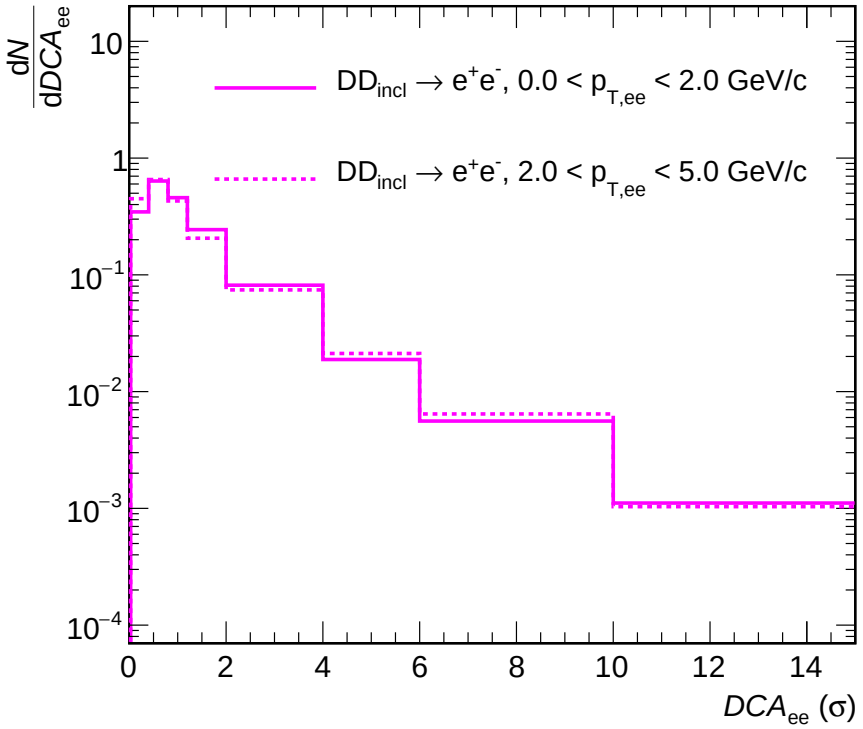

Figure 4.4.: DCA_{ee} spectrum of inclusive D-mesons in two different $p_{\mathrm{T,ee}}$ intervals.

Mode	Decay channel	Effective B.R.
1	$B \to e^+$	11%
2	$B \to \bar{D} \to e^-$	8.5%
3	$B \to \bar{D}e^+ \to e^-e^+$	0.8%

Table 4.2.: B-meson decay channels into electrons and effective branching ratios [PHE 15].

it consistently in MC. In tab. 4.3 the estimated branching ratios for dielectrons from B-mesons are summarized. These branching ratios are now used as weights to calculate an unlike-sign and a like-sign DCA_{ee} spectrum for the dielectrons from B-mesons. The inclusive spectrum is then calculated as the difference between the two and is shown in fig. 4.5.

We can see, that the difference between the spectra is not as striking as for the charged and neutral D-mesons. In 4.6 the $p_{\mathrm{T,ee}}$ dependence for the B-mesons is shown.

We can see, that the spectrum for B-mesons is not a function of the pair transverse momentum.

Modes	B. R. e^+e^-	B.R. $e^-e^- + e^+e^+$
(1)(1)	1.02%	0.19%%
(2)(2)	0.60%	0.12%
(1)(2)	0.30%	1.57%
(3)	1.60%	0.00%

Table 4.3.: Branching ratios for B-mesons into unlike sign and like sign dielectrons considering a probability for $B \to \bar{B}$ oscillation of 20%.

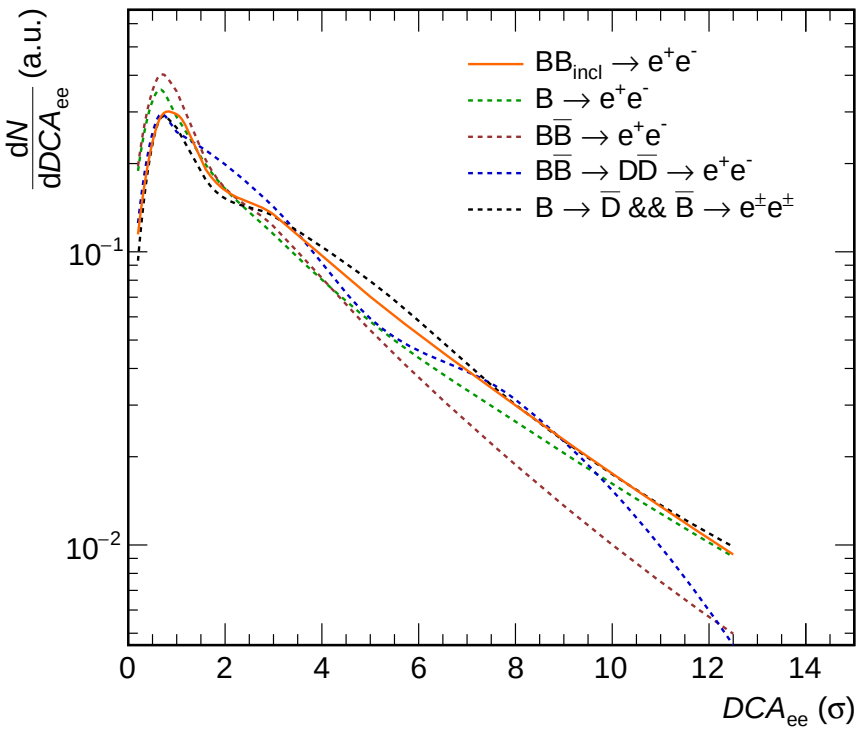

Figure 4.5.: Templates for DCA_{ee} spectra of dielectrons from different B-mesons in MC. Dashed lines are unlike-sign spectra, the solid line is subtracted signal.

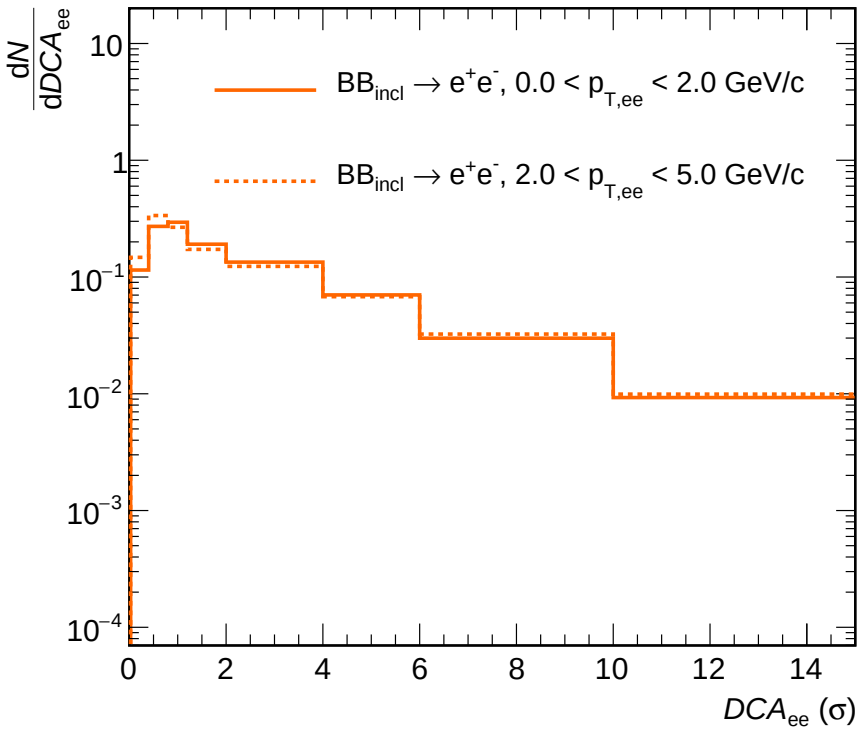

Figure 4.6.: DCA_{ee} spectrum of inclusive B-mesons in two different $p_{\mathrm{T,ee}}$ intervals.

4.2. Cocktail Comparison

In this section we will compare the templates from Monte Carlo to the measured data. To do so we will investigate several mass slices independently. Since there seems to be no evidence for a $p_{\mathrm{T,ee}}$ dependence of the DCA_{ee} spectra the analysis is not differential in this dimension. The templates are normalized to calculations from the hadronic cocktail in the same m_{ee} and $p_{\mathrm{T,ee}}$ range and plot the sum of the normalized templates as well as the single contributions.
The hadronic cocktail is the sum of all known hadronic sources that contribute to the dielectron spectrum. It is calculated via a hybrid event generator based on PYTHIA with an external decayer called EXODUS [ERD 14] [PHE 09]. As input for the calculations measurements are used. The whole input for the hadronic cocktail calculations is summarized in tab. 4.4. The results will be discussed in the next section.

light flavour	π^0, η, K, ϕ, ω	measurement parametrized [ALIc 12] [ALId 12] [ALIf 12]
	η', ρ, ω', ϕ'	m_T scaled from π^0 measurement
heavy flavour	$c\bar{c}$, $b\bar{b}$	measured cross sections [ALIa 12]
	J/ψ	inclusive measurement [ALI 11][ALIe 12]

Table 4.4.: Ingredients for the hadronic cocktail.

4.2.1. Pion Mass Region

The first mass region we are going to look into is the region from 80 MeV/c^2 to 140 MeV/c^2. In this region the π^0 Dalitz decay gives the main contribution to the dielectron spectrum. We do not expect a large contribution from other sources in this mass range which gives us the opportunity to use the pion regime as a control region for this analysis. The result can be seen in fig. 4.7.
One can clearly see, that this mass region is dominated by the π^0 Dalitz decay. The contributions from other sources are negligibly small. Since the scaled template agrees with data within the statistical uncertainties we can argue, that the description of DCA_{ee} in Monte Carlo is correct. The π^0 template will further be used to describe other prompt light-flavour sources.

4.2.2. Resonance Mass Region

The resonance mass region is considered to extend from 160 MeV/c^2 to 1.1 GeV/c^2. It starts after the π^0 mass and ends right behind the ϕ mass. The contributions expected are mainly from η Dalitz, ω and ϕ decays but in this region also a contribution from correlated $\mathrm{e^+e^-}$pairs from D-meson decays is expected. This circumstance makes the resonance region well suited to test if a separation between prompt and non-prompt contributions is possible. The result is shown in fig. 4.8.

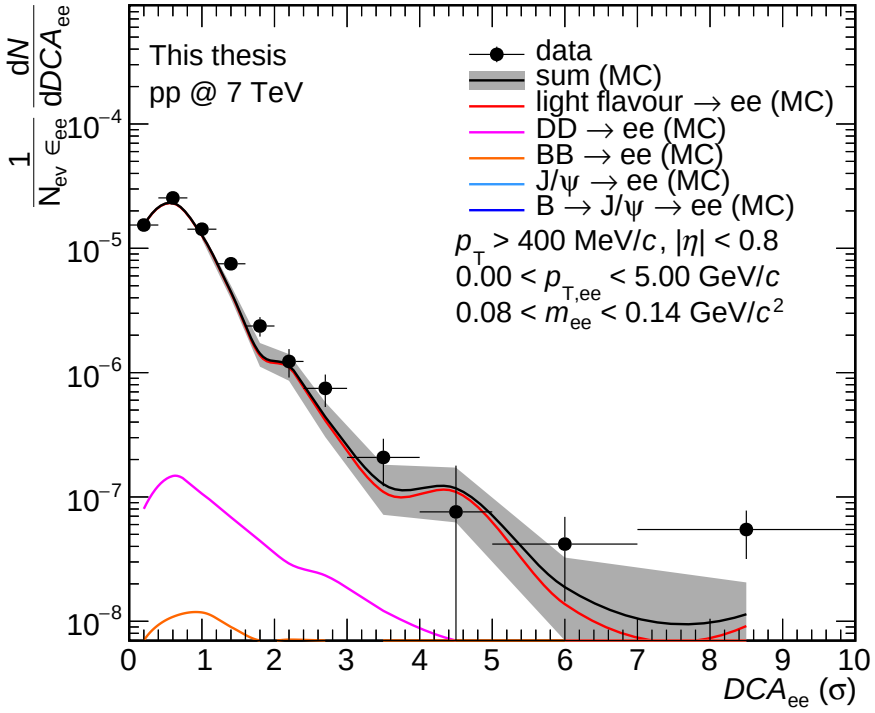

Figure 4.7.: Result for the mass region from 80 MeV/c^2 to 140 MeV/c^2. The data is shown in black dots, the contributions from single particles are drawn in coloured lines, their sum is shown as the black line. The shaded area corresponds to the statistical error of the sum. Data and simulation agree within the statistical errors.

It is clear, that the template for the prompt light-flavour e^+e^- pairs can not describe the data by itself. An additional contribution to describe the tail at large DCA_{ee} is needed. This is accomplished by adding the templates obtained from correlated e^+e^- pairs from D- and B-mesons. With this contributions a good description of the measured data is achieved. This clearly demonstrates the superior resolving power between prompt and non-prompt dielectron sources in this analysis. As such this major achievement constitutes a firm base for further extraction of physical observables.

4.2.3. Intermediate Mass Region

The intermediate-mass region is considered between 1.1 GeV/c^2 and 2.7 GeV/c^2. With this selection the contribution from either the ϕ or the J/ψ should be negligible. The comparison of data, and cocktail-scaled templates is shown in fig. 4.9.

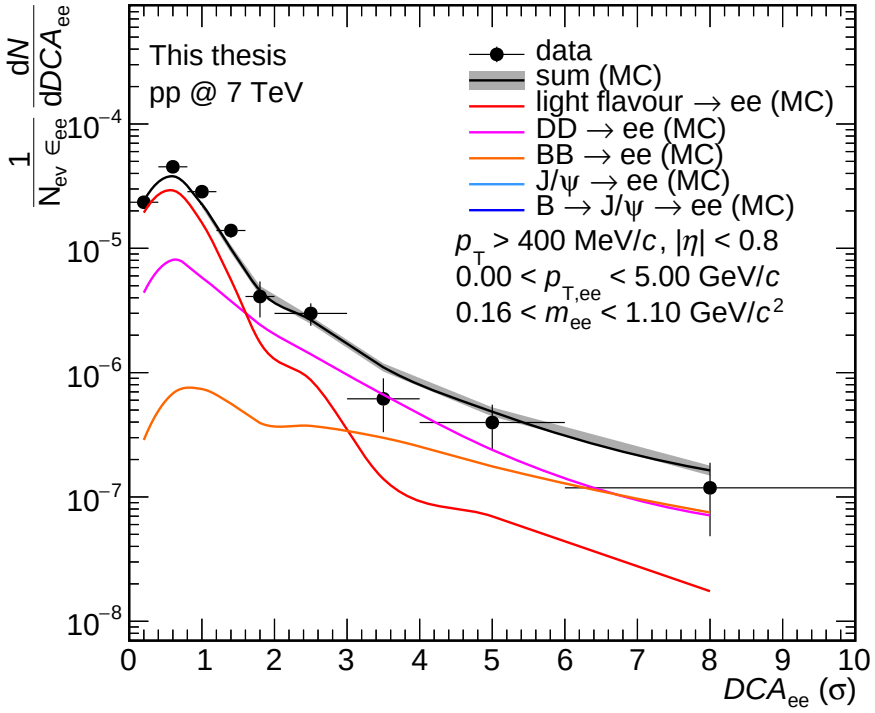

Figure 4.8.: The sum over the normalized single contributions is plotted as a black line. The light flavour template with addition of the heavy flavour leads to a nice description of the data.

A good description in this region is apparent. The contributions from light-flavour decays and the J/ψ are very small as expected. In particular, no significant contribution from a prompt thermal source can be observed. Generally, there should be no contribution from the J/ψ in this region, since its mass is 3.096 GeV/c^2[CPC 14] and its a very narrow peak in the mass spectrum. The small contribution from the J/ψ is due to bremsstrahlung effects, where the electrons lose momentum while traversing material. This leads to a smaller reconstructed mass. This effect is included in the cocktail.

4.2.4. J/ψ Mass Region

In the J/ψ mass region we have another opportunity to look into the distributions from expected prompt and non-prompt contributions. The prompt part stemming from the decay of J/ψ produced in binary collisions and the non-prompt from feed down of B-

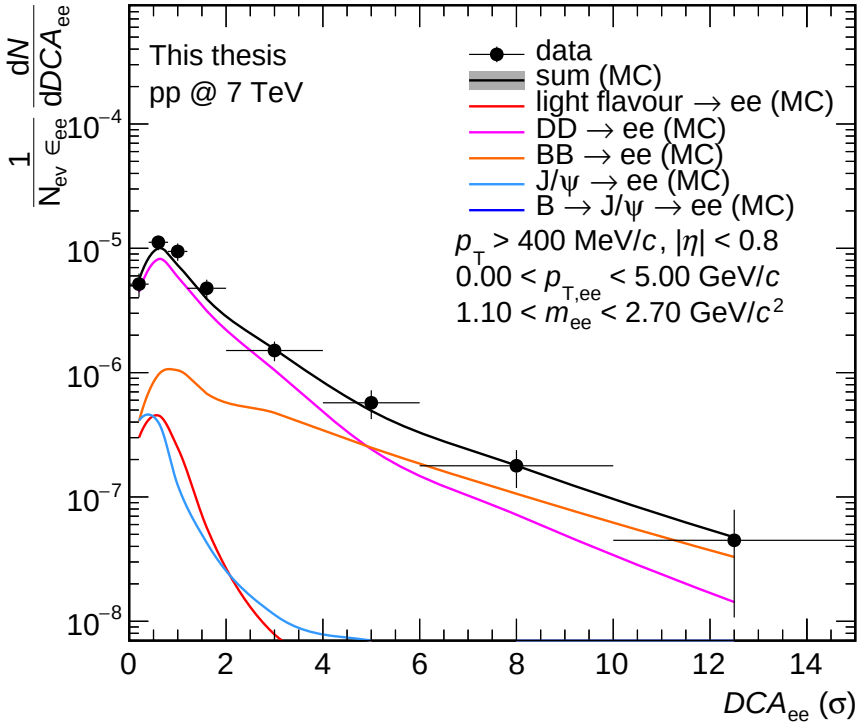

Figure 4.9.: Comparision of data and monte carlo in the intermediate-mass region.

mesons which decay into J/ψ which then decays into a e^+e^- pair. The comparison of data and the normalized templates is shown in fig. 4.10.

The templates describe the data within statistical uncertainties. We can see, that the peak in the spectrum is reproduced by the prompt J/ψ. The contribution from $B \rightarrow$ J/ψ gives a good description of the tail of the spectrum but the addition of the other heavy-flavour contributions is needed to match the data points. Without correlated e^+e^- pairs from the semileptonic decays of D- and B-meson the simulation would undershoot the measurement at large DCA_{ee} in this mass region. The normalization for prompt and non-prompt J/ψ are obtained from inclusive measurements and then scaled with the measured fraction of beauty hadrons decaying via the J/ψ channel $h_B \rightarrow$ prompt J/ψ = 0.149 published by the ALICE collaboration [ALIa 12].

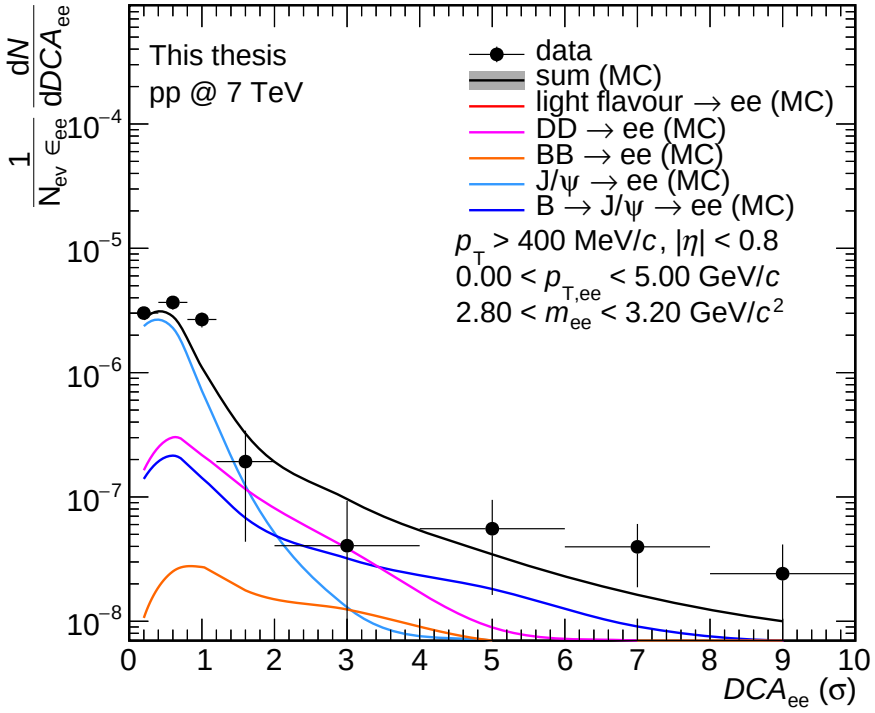

Figure 4.10.: Comparison of data and cocktail-scaled templates in the Jpsi mass region. The fraction of $\frac{B\to J/\psi}{\text{prompt J}/\psi}$ was measured in ALICE to be 0.149 [ALIa 12] and was applied here.

4.3. Discussion

In the previous chapter it was shown that the studied mass regions can all be described by the Monte Carlo templates. From this we can conclude, that the description of the DCA_{ee} spectra in Monte Carlo is reasonable. Since the templates were scaled to the integral of the hadronic cocktail in the corresponding mass region we can show, that the cocktail method gives feasible results. The integrated yields in all mass regions are summarized in tab. 4.3.

We can clearly see that the cocktail slightly undershoots the data. This might have several reasons. For one also a virtual direct photon contribution is not included in the cocktail. These photons from hard scattering of quarks and gluons might be responsible for a part of the missing yield. Another argument is that the normalization from the hadronic cocktail is not completely right. A problem in the light-flavour regime is probably the kinematic range in which e.g. the pions are measured and therefore the description at low p_T. In the

Mass region	raw yield in data	raw yield in MC	data/MC
0.08 – 0.14 GeV/c^2	$2.75 \cdot 10^{-5} \pm 8.0 \cdot 10^{-7}$	$2.39 \cdot 10^{-5} \pm 8.0 \cdot 10^{-7}$	1.15 ± 0.05
0.16 – 1.10 GeV/c^2	$5.10 \cdot 10^{-5} \pm 1.8 \cdot 10^{-6}$	$4.50 \cdot 10^{-5} \pm 1.0 \cdot 10^{-6}$	1.13 ± 0.05
1.10 – 2.70 GeV/c^2	$1.92 \cdot 10^{-5} \pm 1.4 \cdot 10^{-6}$	$1.73 \cdot 10^{-5} \pm 2.0 \cdot 10^{-7}$	1.11 ± 0.08
2.80 – 3.20 GeV/c^2	$4.22 \cdot 10^{-6} \pm 3.3 \cdot 10^{-7}$	$3.22 \cdot 10^{-6} \pm 1.0 \cdot 10^{-8}$	1.31 ± 0.10

Table 4.5.: Raw yields and ratios of data and Monte Carlo in the single mass regions.

heavy flavour the already mentioned large uncertainties of the charm contribution should also be taken into account when looking into the intermediate and J/ψ mass regions.
In the J/ψ mass region we might also have a dependence on which model is used to generate the initial events. This could lead to a slightly different p_{T} distribution in the MC sample. As it was shown this should only concern the $B \rightarrow$ J/ψ decays but could lead to a better description in the tail.
Looking into the resonance mass distributions we could clearly show, that DCA_{ee} gives a good handle on distinguishing prompt from non-prompt pairs. This is what will be needed for a measurement of the thermal photon contribution in the intermediate mass region.

5. Summary and Outlook

The comparisons of the constructed templates with the measured data shows that the overall shape of the templates describes the data. This shows us that the description of DCA_{ee} in MC is reasonable. Investigating the integrated yields from data and Monte Carlo we saw that there might still be problems in the hadronic cocktail. These were discussed and probable reasons for this discrepancy were given. In the end we could conclude that the method developed in this analysis could provide the needed tools for a future measurement of virtual thermal photons.
The next steps would be to start studying additional collision systems with this analysis. In case of pp we can not expect to find a thermal photon component. So the final goal would be to use this method in the case of Pb–Pb and measure the temperature of the QGP. However, there are more possibilities for application. One would be to leave the absolute normalization as a free parameter and use the templates to extract the cross-section for $c\bar{c}$ and $b\bar{b}$ production.
The upgrade of the ALICE experiment will also give new perspectives for this analysis. As indicated by statistical uncertainties on the data points one challenge of this analysis is the statistics. Here the upgrade of the TPC readout chambers from the MWPCs to a GEM based system will give the possibility of a continuous read out of the TPC. This will lead to a drastic improvement in statistics. Also the ITS will be upgraded. Here a factor of two considering the resolution of the DCA for tracks will be achieved. The resolution is essentially the limiting factor in this measurement. This also means, that the separation between prompt and non-prompt e^+e^- pairs will get a better. The combination of improved statistics and DCA_{ee} resolution will allow for a detailed study of thermal dielectrons from the QGP in the intermediate-mass region.

A. Appendix

A.1. Units

The standard unit for measuring length in particle and high energy physics is the so called femtometer or 'fermi' (1 fm = 10^{15} m). One fermi is approximately the diameter of a proton. Since macroscopic energies are rare in high energy physics the unit joule is replaced bi the electronvolt (eV).

$$1 \text{ eV} = e \cdot 1 \text{ V} = 1.6022 \cdot 10^{-19} \text{ C} \cdot 1 \text{ V} = 1.6022 \cdot 10^{-19} \text{ J} \tag{A.1}$$

Following Einsteins's $E = mc^2$ it is common in particle and high energy physicsn to give masses and momentum in orders of eV/c^2 or eV/c respectively.

A.2. Kinematics

In the following section the basic kinematic variables are introduced and discussed. The 4 momentum of a particle is given by

$$p^\mu = \left(\frac{E}{c}, \mathbf{p}\right) \tag{A.2}$$

where E is the particles energy and $\mathbf{p}$ its 3 momentum. The relativistic energy-momentum relation is given bympuls-Beziehung gegeben

$$E = \sqrt{m_0^2 c^4 + p^2 c^2}, \tag{A.3}$$

with m_0 as the rest mass of the particle. The used coordinate system is oriented such that the z-axis points into beam direction and the x- and y-axis span the azimuthal plane to the beam-axis. Now it is possible to disentangle the 3 momentum vector into its transversal(azimuthal) and its longitudinal(beam-axis) part.

$$\mathbf{p} = p_\parallel + p_\perp, \tag{A.4}$$

with

$$p_\parallel = p_z = p_L = |\mathbf{p}| \cdot \cos(\theta) \text{ and} \tag{A.5}$$

$$p_\perp = p_T = \sqrt{p_x^2 + p_y^2} = |\mathbf{p}| \cdot \sin(\theta). \tag{A.6}$$

θ equates here to the angle between the beam-axis and the particles momentum vector. The angle between the x and y component of the momentum is denoted as φ and gives the azimuthal direction. I will further use the notaion p_L and p_T. The transverse mass is defined as

$$m_\mathrm{T} = \sqrt{p_\mathrm{T}^2 + m_0^2} \tag{A.7}$$

From these quantities new ones can be constructed.

$$\text{Rapidity}: y = \frac{1}{2} \ln\left(\frac{E + p_\mathrm{L}}{E - p_\mathrm{L}}\right) = \ln\left(\frac{E + p_\mathrm{L}}{m_\mathrm{T}}\right) = \tanh^{-1}\left(\frac{p_\mathrm{L}}{E}\right) \tag{A.8}$$

The rapidity is not orthogonal to p_x and p_y and also not Lorentz invariant, but has the advantage that the shape of its distribution does not change under Lorentz transformation.

$$\text{Pseudo rapidity}: \eta = \frac{1}{2} \ln\left(\frac{|\mathbf{p}| + p_\mathrm{L}}{|\mathbf{p}| - p_\mathrm{L}}\right) = -\ln\left(\tan\left(\frac{\theta}{2}\right)\right) \tag{A.9}$$

In contrast to rapidity the shape of the pseudo-rapidity distribution depends on the frame of reference, but has the advantage, that one only needs to measure an angle to determine it which makes particle identification unnecessary. Other important relations are:

$$E = m_\mathrm{T} \cdot \cosh(y) \tag{A.10}$$

$$p_L = m_\mathrm{T} \cdot \sinh(y) \tag{A.11}$$

$$\mathbf{p} = p_\mathrm{T} \cdot \cosh(\eta) \tag{A.12}$$

$$p_L = p_\mathrm{T} \cdot \sinh(\eta) \tag{A.13}$$

A.3. Coordinates in ALICE

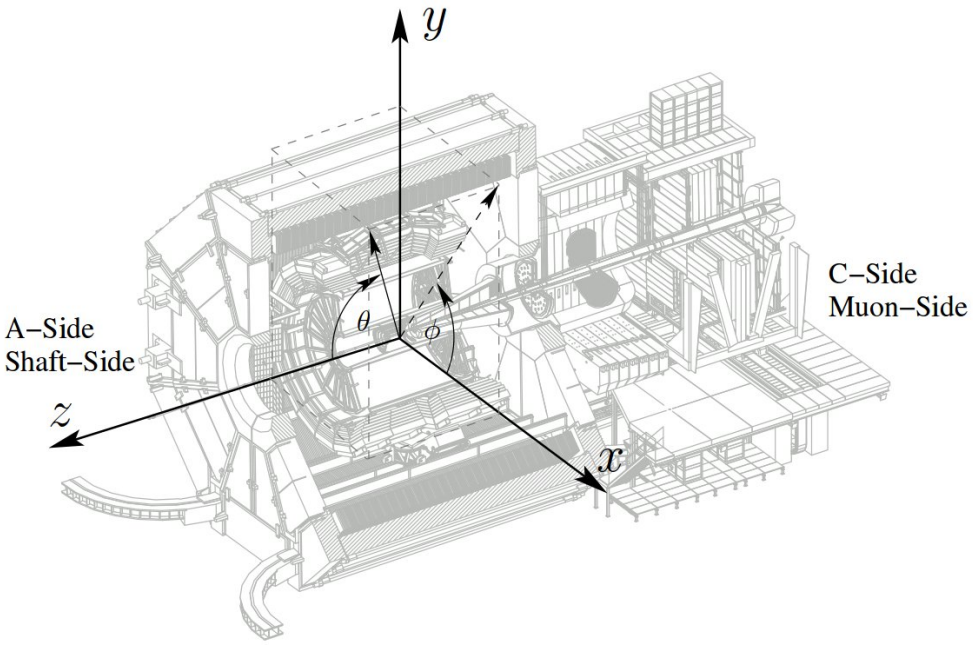

Figure A.1.: Schematic drawing of the ALICE detector with the definition of the coordinate system used in the experiment [Wie 08].

A.4. List of Runs

LHC10b

117222, 117220, 117116, 117112, 117109, 117099, 117092, 117063, 117060, 117059, 117053, 117052, 117050, 117048, 116787, 116645, 116643, 116574, 116571, 116562, 116432, 116431, 116429, 116403, 116402, 116372, 116360, 116358, 116288, 116102, 116081, 116079, 115414, 115406, 115401, 115399, 115393, 115369, 115345, 115335, 115328, 115327, 115322, 115318, 115312, 115310, 115193, 115186, 115056, 114931, 114930, 114924, 114920, 114918, 114798, 114786

LHC10c

121040, 121039, 120829, 120825, 120824, 120823, 120822, 120821, 120758, 120750, 120741, 120671, 120617, 120616, 120505, 120504, 120503, 120244, 120079, 120076, 120073, 120072, 120069, 120067, 119862, 119859, 119856, 119853, 119849, 119846, 119845, 119844, 119842, 119841, 118561, 118560, 118558, 118556, 118518, 118512, 118507, 118506

LHC10d

126432, 126425, 126424, 126422, 126409, 126408, 126407, 126406, 126405, 126404, 126403, 126359, 126352, 126351, 126350, 126285, 126284, 126283, 126168, 126167, 126160, 126158,

126097, 126090, 126088, 126082, 126081, 126078, 126073, 126008, 126007, 126004, 125855, 125851, 125850, 125849, 125848, 125847, 125844, 125843, 125842, 125633, 125632, 125630, 125628, 125296, 125295, 125186, 125156, 125140, 125139, 125134, 125133, 125101, 125100, 125097, 125085, 125083, 125023, 124751, 122375, 122374

LHC10e

130850, 130848, 130847, 130844, 130842, 130840, 130834, 130799, 130798, 130795, 130793, 130704, 130696, 130628, 130623, 130621, 130620, 130609, 130608, 130526, 130524, 130520, 130519, 130517, 130481, 130480, 130479, 130375, 130360, 130358, 130356, 130354, 130342, 130178, 130172, 130168, 130158, 130157, 130149, 129983, 129966, 129962, 129961, 129960, 129744, 129742, 129738, 129736, 129735, 129734, 129729, 129726, 129725, 129723, 129666, 129659, 129653, 129652, 129651, 129650, 129647, 129641, 129639, 129599, 129587, 129586, 129540, 129536, 129528, 129527, 129525, 129524, 129523, 129521, 129520, 129519, 129516, 129515, 129514, 129513, 129512, 129042, 128913, 128855, 128853, 128850, 128843, 128836, 128835, 128834, 128833, 128824, 128823, 128820, 128819, 128778, 128777, 128678, 128677, 128621, 128615, 128611, 128609, 128605, 128596, 128594, 128592, 128582, 128506, 128505, 128504, 128503, 128498, 128495, 128494, 128486, 128452, 128366

LHC10f

134927, 134297, 133982, 133969, 133920, 133800, 133762, 133670, 133563, 133414, 133330, 133329, 133327, 133010, 133007, 133006

Bibliography

[ALI 99] ALICE Collaboration, *Technical Design Report of the Inner Tracking System*, CERN/LHCC 99–12, 1999.

[ALI 11] ALICE Collaboration, *Rapidity and transverse momentum dependence of inclusive* J/ψ *production in pp collisions at sqrts = 7 TeV*, Phys. Lett. B 704, 442-455, 2011

[ALI 12] ALICE Collaboration, *Upgrade of the ALICE Experiment Letter Of Intent*, J. Phys. G: Nucl. Part. Phys. 41 087001, 2014

[ALIa 12] ALICE Collaboration, *Measurement of prompt* J/ψ *and beauty hadron production cross sections in mid-rapidity in pp at* $\sqrt{s}$ *= 7 TeV*, arXiv:1205.5880v2 [hep-ex], 2012.

[ALIb 12] ALICE Collaboration, *Measurement of charm production at central rapidity in proton-proton collisions at* $\sqrt{s} = 2.76$ *TeV*, arXiv:1205.4007 [hep-ex], 2012.

[ALIc 12] ALICE Collaboration, *Neutral pion and* η *meson production in proton-proton collisions at* $\sqrt{s}$ *= 0.9 TeV and* $\sqrt{s} = 7TeV$, arXIv: 1205.5724 [hep-ex], 2012

[ALId 12] ALICE Collaboration, *Production of K*(892) and* ϕ*(1020) in pp collisions at* $\sqrt{s}$*=7 TeV*, arXiv: 1208.5717 [hep-ex], 2012

[ALIe 12] ALICE Collaboration, *Erratum to "Rapidity and transverse momentum dependence of inclusive* J/ψ *production in pp collisions at sqrts = 7 TeV" [Phys. Lett. B 704 (5) (2011) 442]*, Phys. Lett. B 704, 692-698, 2012

[ALIf 12] ALICE Collaboration, $\omega \rightarrow \pi^0\pi^+\pi^-$ *) in p+p collisions at* $\sqrt{s}$*=7 TeV*, ALICE internal note

[ALI 14] ALICE Collaboration, *Performance of the ALICE Experiment at the CERN LHC*, Int. J. Mod. Phys. A 29, 1430044, 2014

[ALI 15] ALICE Collaboration, *Measurement of pion, kaon and proton production in proton-proton collisions at $\sqrt{s}$ = 7 TeV*,
arXiv: 1504.00024 [nucl-ex], 2015

[AKI 13] A. Akindinov it et al., *Performance of the ALICE Time-Of-Flight detector at the LHC*,
Eur. Phys. J. Plus (2013) 128:44, 2013

[ALM 10] J. Alme *et al.*, *The ALICE TPC, a large 3-dimensional tracking device with fast readout for ultra-high multiplicity events*, Nucl.Instrum.Meth. A622 (2010) 316-367, 2010

[ATL 12] ATLAS Collaboration, *Observation of a new particle in the search for the Standard Model Higgs boson with the ATLAS detector at the LHC*,
Phys. Lett. B, Volume 716, Issue 1, 2012

[BEO 12] S. Beolé, for the ALICE Collaboration, *The ALICE Inner Tracking System: Performance with Proton and Lead Beams*,
Physics Procedia Volume 37, Pages 1062-1069, 2012

[BMS 96] P. Braun-Munzinger, J. Stachel, *Probing the Phase Boundary between Hadronic Matter and the Quark-Gluon-Plasma in Relativistic Heavy Ion Collisions*,
arXiv:9606017 [nucl-th], 1996.

[BRR 10] W. Blum, W. Riegler, L. Rolandi, *Particle Detection with Drift Chambers*,
Springer-Verlag Berlin Heidelber, 2010

[CMS 12] CMS Collaboration, *Observation of a new boson at a mass of 125 GeV with the CMS experiment at the LHC*,
Phys. Lett. B, Volume 716, Issue 1, 2012

[CMS 15] CMS Collaboration, *Measurement of the inclusive 3-jet production differential cross section in proton–proton collisions at 7 TeV and determination of the strong coupling constant in the TeV range*,
Eur. Phys. J. C 75: 186. doi:10.1140/epjc/s10052-015-3376-y, 2015

[CPC 14] K. A. Olive *et. al.* (Particle Data Group), *Review of particle physics*,
Chinese Physics C 38/9, 2014.

[EHB 16] S. Endres, H. van Hees, M. Bleicher, *Energy, centrality and momentum dependence of dielectron production at collider energies in coarse-grained transport approach*,
arXiv: 1604.06415v2 [nucl-th], 2016.

[ERD 14] I. Erdemir Özdemir, *Dielectron cocktail simulation in pp, p–Pb and Pb–Pb collisions at LHC energies*,
Master thesis, Frankfurt, 2014

[FK 04] Z. Fodor, S. D. Katz, *Critical point of QCD at finite T and μ, lattice results for physical quark masses*,
JHEP, 04, 050 doi: http://stacks.iop.org/1126-6708/2004/i=04/a=050, 2004.

[JHS 16] J. H. Stiller, *Full kinematic reconstruction of charged B mesons with the upgraded Inner Tracking System of the ALICE Experiment*,
Doctoralthesis, University of Heidelberg, 2016

[KSSS 08] M. Kliemant, R. Sahoo, T. Schuster, R. Stock, *Global Properties of Nucelus-Nucleus Collisions*,
arXiv:0809.2482 [nucl-ex], 2008.

[KW 55] N. M. Kroll, W. Wada, *Internal Pair Production Associated with the Emission of High-Energy Gamma Rays*,
Phys. Rev. 98, 1355, doi: http://dx.doi.org/10.1103/PhysRev.98.1355, 1955.

[LIP 11] C. Lippmann, *Particle identification*,
arXiv: 1101.3276, 2011.

[LMW 95] P. Lévai B. Müller, X-N Wang, *Open charm production in an equilibrating parton plasma*,
Phys. Rev C51, 3326, 1995.

[NA60 08] NA60 Collaboration, *Evidence for the production of thermal muon pairs with masses above 1GeV/c^2 in 158 A GeV Indium-Indium colissions*,
arXiv: 0810.3204v2 [nucl-ex], 2008.

[NAG 07] J. L. Nagel, *The letter "s" (and the sQGP)*,
Eur. Phys. J. C 49, 275–279, 2007

[PHE 09] PHENIX Collaboration, *Detailed measurement of the e^+e^- pair continuum in p+p and Au+Au collisions at $\sqrt{s_{NN}}$= 200 GeV and implications for direct photon production*,
arXiv:0912.0244v1 [nucl-ex], 2009

[PHE 15] PHENIX Collaboration, *Formation of dense partonic matter in relativistic nucleus-nucleus collisions at RHIC: Experimental evaluation by the PHENIX collaboration*,
Nucl. Phys. A757 , 184-283, 2015

[PHE 15] PHENIX Collaboration, *Cross section for $b\bar{b}$ production via dielectrons in d+Au collisions at $\sqrt{s_{NN}}$= 200 GeV*,
Phys. Rev. C 91, 014907, DOI: http://dx.doi.org/10.1103/PhysRevC.91.014907, 2015.

[PRE 12] R. Preghenella, ALICE figure repository, 2012.

[RAP 11] R. Rapp, *Theory of Soft Electromagnetic Emission in Heavy-Ion Collisions*, arXiv: 1110.4345v1 [nucl-th], 2011.

[REI 16] P. S. Reichelt, private communication, 2016.

[SSS 10] S. Sarkar, H. Satz, B. Sinha, (Eds.), *The Physics of the Quark-Gluon Plasma: Introductory Lectures*,
Springer, Berlin Heidelberg, 2010.

[SRS 98] M. Stephanov, K. Rajagopal, E. Shuryak, *Signatures of the Tricritical Point in QCD*,
Phys. Rev. Lett. 81, 4816, DOI: https://doi.org/10.1103/PhysRevLett.81.4816, 1998.

[Wie 08] J. Wiechula, *Commisioning and Calibration of the ALICE-TPC*,
Ph. D. Thesis, Frankfurt, 2008.

Danksagung

Zuallererst möchte ich Professor Harald Appelshäuser für die Möglichkeit meine Masterarbeit in der Frankfurter ALICE Arbeitsgruppe zu schreiben und seine Unterstützung dabei danken.

Theo Bröker und Patrick Reichelt und der Dielektronengruppe danke ich für zahlreiche Hilfestellungen und anregende Diskussionen.
Ich bedanke mich bei der gesamten Frankfurter ALICE Arbeitsgruppe für die interessanten Diskussionen, Hilfestellungen jedweder Art und das hervorragende Arbeitsklima. An dieser Stelle sollten auch einige Personen die am HADES und CBM Experiment arbeiten nicht vergessen werden.

Nicht zuletzt danke ich meiner Familie für ihre Unterstützung in jeglicher Hinsicht, ohne die mein Studium nur schwer möglich gewesen wäre.

Erklärung

nach § 28 (12) Ordnung für den Bachelor- und den Masterstudiengang Physik

Hiermit erkläre ich, dass ich diese Arbeit selbstständig und ohne Benutzung anderer als der angegebenen Quellen und Hilfsmittel verfasst habe. Alle Stellen der Arbeit, die wörtlich oder sinngemäß aus Veröffentlichungen oder aus anderen fremden Texten entnommen wurden, sind von mir als solche kenntlich gemacht worden. Ferner erkläre ich, dass diese Arbeit nicht - auch nicht auszugsweise - für eine andere Prüfung verwendet wurde.

Sebastian Scheid, Frankfurt am Main, den 24. Oktober 2016